Journal of Baku Engineering University

PHYSICS

ISSN 2521-6368

Volume 9
Number 1
2025

Journal is published twice a year
Number - 1. June, Number - 2. December

An International Journal

http://journal.beu.edu.az

Contact address
Journal of Baku Engineering University
AZ0102, Khirdalan city, Hasan Aliyev str. 120, Absheron, Baku, Azerbaijan
Tel: *00 994 12 - 349 99 95* ***Fax:*** *00 994 12 349-99-90/91*

e-mail: *jr-phisics@beu.edu.az*
web: *http://journal.beu.edu.az*
facebook: *Journal Of Baku Engineering University*

ISSN 2521-6368

ISSN 2521-6368

Journal of Baku Engineering University

PHYSICS

Baku - AZERBAIJAN

Journal of Baku Engineering University

PHYSICS

2025. Volume 9, Number 1

CONTENTS

JOURNAL OF BAKU ENGINEERING UNIVERSITY - PHYSICS
2025. Volume 9, Number 1 *Pages 3-9*

UDC 539.23:537.311.33
DOI: https://doi.org/10.30546/09081.2025.001.8010

FIRST-PRINCIPLES INVESTIGATION OF CHIRALITY-DEPENDENT ELECTRONIC PROPERTIES IN CARBON NANOTUBES

Vusala Nabi JAFAROVA[1,2*], Khayala Ajdar HASANOVA[3,1], Sevda RZAYEVA[3,4], Razim Baba BAYRAMLI[5]

[1]*Azerbaijan State Oil and Industry University, 20 Azalig Ave., AZ-1010, Baku, Azerbaijan*

[2]*Khazar University, 41 Mehseti Str., AZ 1096, Baku, Azerbaijan*

[3]*Ministry of Science and Education Republic of Azerbaijan, Institute of Physics, 131 H. Javid Ave., AZ-1143, Baku, Azerbaijan*

[4]*Azerbaijan State University of Economics (UNEC), 6 Istiglaliyyat Str., AZ-1001, Baku, Azerbaijan*

[5]*Baku Engineering University, Khirdalan city, Hasan Aliyev str., 120 AZ-0101, Absheron, Azerbaijan*

ARTICLE INFO

Article history:
Received 2025.05.09
Received in revised form 2025.06.19
Accepted:2025-07-03
Available online

Keywords:

Chiral vector;
Band structure;
Density of states;
Fermi level;
Ab initio modeling

ABSTRACT

The electronic properties of single-walled carbon nanotubes (SWCNTs) are strongly influenced by their chirality, which plays a crucial role in determining their suitability for applications in nanoelectronics, energy storage, and other advanced technologies. In this study, we present an ab initio modeling framework for predicting the Fermi energy distribution in SWCNTs as a function of their chiral indices. Using first-principles calculations based on density functional theory (DFT), we systematically investigate the electronic structures of SWCNTs with chiral vectors (n, m), where n = 4, 5, 6 and m = 0. Our results indicate that these specific chiralities yield metallic behavior, as evidenced by the absence of a band gap. This computational approach provides fundamental insights into the chirality-dependent electronic behavior of carbon nanotubes, thereby supporting the rational design of carbon-based nanomaterials tailored for specific electronic applications.

[*]*Corresponding author. E-mail address: vusala.cafarova@asoiu.edu.az*

1. Introduction

Single-walled carbon nanotubes (SWCNTs) have attracted significant interest due to their exceptional electronic properties, which are highly sensitive to their chirality—the geometric arrangement of carbon atoms defined by chiral indices (n,m) [1,2]. This chirality dependence directly impacts their classification as metallic or semiconducting; with armchair nanotubes consistently exhibiting metallic behavior, while zigzag and chiral variants display either semiconducting or metallic properties depending on specific chiral values [3,4]. These characteristics make SWCNTs highly suitable for integration into nanoelectronic, energy storage, and sensing devices [5].

Traditional *ab initio* approaches, such as density functional theory (DFT), have been widely used to explore the electronic structure of SWCNTs with various chiralities [6,7].

While DFT provides accurate insight into band structure and Fermi energy distributions, it is computationally intensive, especially when extended to a large and diverse set of nanotube configurations [8]. To address this limitation, our study introduces a hybrid modeling framework that integrates DFT-based calculations with machine learning techniques to predict the Fermi energy distribution in SWCNTs as a function of chirality. Specifically, we focus on nanotubes with chiral vectors (n,0) for n=4, 5, 6, representing a class of zigzag SWCNTs known for their metallic behavior under certain conditions.

The proposed approach not only reduces the computational cost associated with large-scale quantum mechanical simulations but also captures underlying trends in the electronic behavior of carbon nanotubes with varying chiralities. By accurately modeling the Fermi energy across different structural configurations, our method provides a scalable pathway for the rational design of SWCNT-based nanomaterials tailored for specific technological applications in electronics, optoelectronics, and energy systems [9,10].

2. Computational Methods

This study combines ab-initio modeling to predict the Total Density of States (TDOS) distribution in single-walled carbon nanotubes (SWCNTs) with varying chirality, specifically from (4,0) to (6,0). The simulations were performed using Density Functional Theory (DFT), implemented in the Atomistic Tool Kit - Virtual Nano Laboratory (ATK-VNL) code. The Local Density Approximation (LDA) within DFT was employed for the calculations.

The Carbon-Carbon bond length was set to 1.42 Å. For each CNT system, chiral configurations ranging from (4,0) to (6,0) were generated to study how the band gap varies with the chirality of the nanotubes. The electron-ion and electron-electron interactions were treated using FHI ionic pseudopotentials and predefined Perdew-Zunger (PZ) functionals.

For the single-walled chiral CNTs with indices (n=4-6; m=0), Monkhorst-Pack (MP) grids of 1×1×5 k-sampling were used. All atomic positions were geometrically optimized during the calculations. Carbon atoms were considered with a valence configuration of C + [He] $2s^2$ $2p^2$, and a kinetic energy cutoff of 50 Ha was employed to ensure full convergence of the total energy calculations. The convergence criteria for the geometry optimization of the studied nanostructures, which contain 16, 20, and 24 atoms, were set to force tolerances of no higher than 0.05 eV/Å and stress tolerances of 0.1 GPa.

1. Results and Discussion

3.1. Electronic properties of CNT

Several studies have been devoted to investigating the electronic properties of single-walled chiral carbon nanotubes (SWCNTs). In Ref. [7], the authors reported first-principles calculations of the electronic properties of SWCNTs with chiralities (6,0) and (8,0) using Density Functional Theory (DFT) implemented in the Vienna Ab Initio Simulation Package (VASP). Matsuda et al. [8] conducted ab initio quantum mechanical predictions of electronic band structures for SWCNTs with zigzag structures using the B3LYP functional within DFT. Barone et al. [9] also examined optical properties of SWCNTs with DFT-LDA, DFT-PBA, and DFT-B3LYP simulations, noting that LDA and GGA functionals generally yielded lower values (~0.4 eV) compared to B3LYP. The experimental analysis of the electronic properties of SWCNTs from scanning tunneling microscopy (STM) measurements shows that the zigzag structure with (9,0) chirality exhibits a band gap of 0.080 ± 0.005 eV [10], which agrees with our results.

In this section, we calculated the electronic band structures, total density of states (TDOS), and partial density of states (PDOS) for SWCNTs with various diameters, specifically for chiralities (n=4, 5, 6; m=0). It is well-known that many physical and chemical properties of SWCNTs are highly dependent on their chirality, and these properties do not exhibit a simple monotonic trend. The band gap of SWCNTs can range from 0 eV to approximately 2 eV, and these nanotubes can either exhibit semiconducting or metallic behavior. CNTs are not strictly semi-metallic because the degeneracy point is slightly shifted from the K symmetry point in the Brillouin zone (BZ). This results in the π-bonding and π*-anti-bonding energy bands meeting at the Fermi level, causing the band gap to approach zero eV. This behavior arises due to the curvature of the nanotube surface, which induces hybridization between the σ*- and π*-anti-bonding energy bands, modifying the electron band dispersions. Based on the computed electronic band structures, we estimated the band gap for all studied 1D SWCNT nanosystems with chiralities ranging from (4,0) to (6,0). Our first-principles calculations indicate that the SWCNTs containing 16, 20, and 24 atoms exhibit metallic characteristics with a band gap of 0 eV, in agreement with recent computational studies.

Table 1. First principles results for single walled CNT systems with different chirality

System	Chirality	Diameter, Å		Band gap, eV	
		This work	Ref.	This work	Ref.
C_{16}	(4,0)	3.13	-	0	-
C_{20}	(5,0)	3.98	-	0	0 **[8]**
C_{24}	(6,0)	4.70	4.76 [7] 4.89 [8]	0	0 [7]

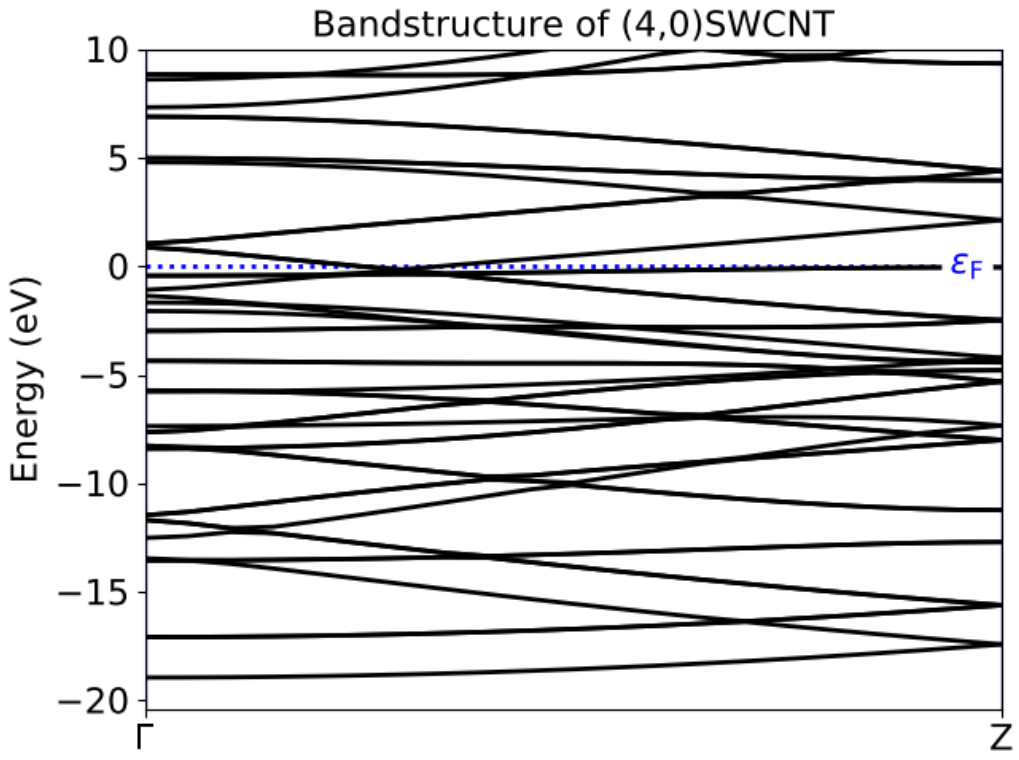

Fig. 1 First-principles calculated band structure for SWCNT with chirality (4,0)

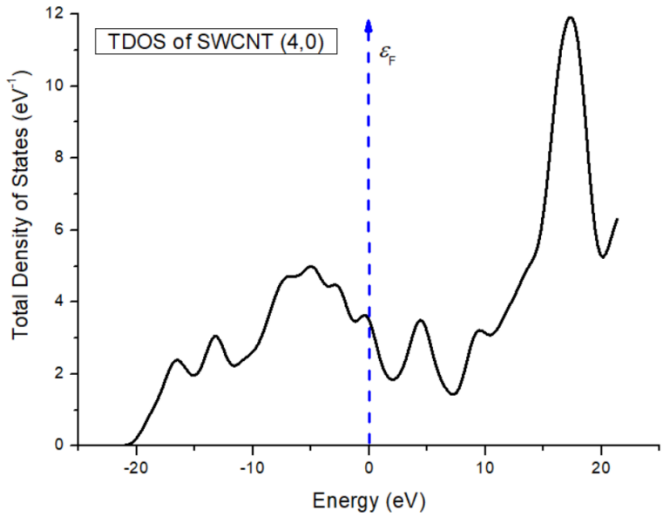

Fig. 2 First-principles calculated total density of states for SWCNT with chirality (4,0)

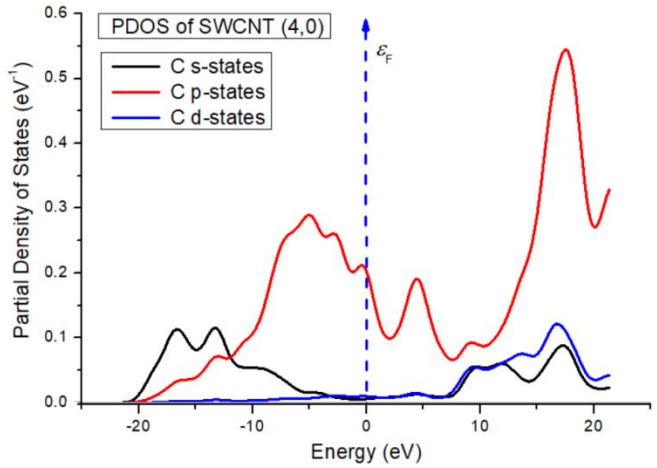

Fig. 3 First-principles calculated partial density of states of carbon in SWCNT with chirality (4,0)

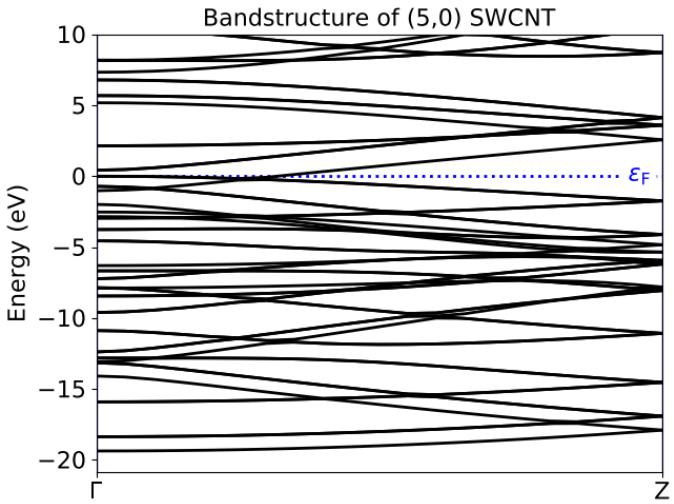

Fig. 4 First-principles calculated band structure for SWCNT with chirality (5,0)

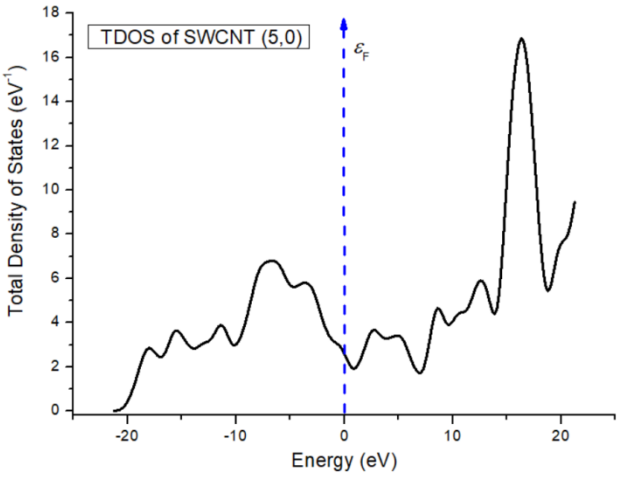

Fig. 5 First-principles calculated total density of states of SWCNT with chirality (5,0)

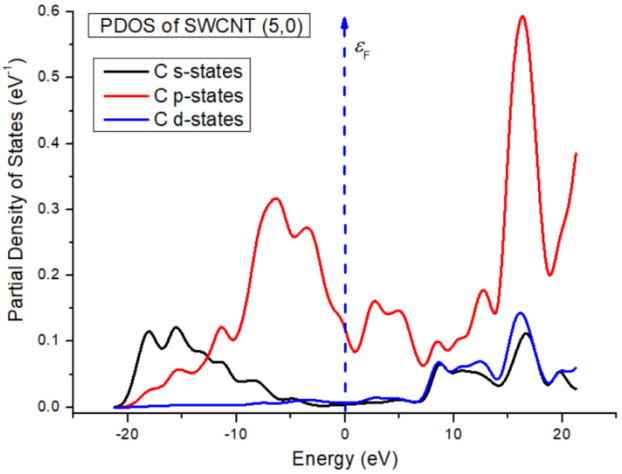

Fig. 6 First-principles calculated partial density of states of carbon in SWCNT with chirality (5,0)

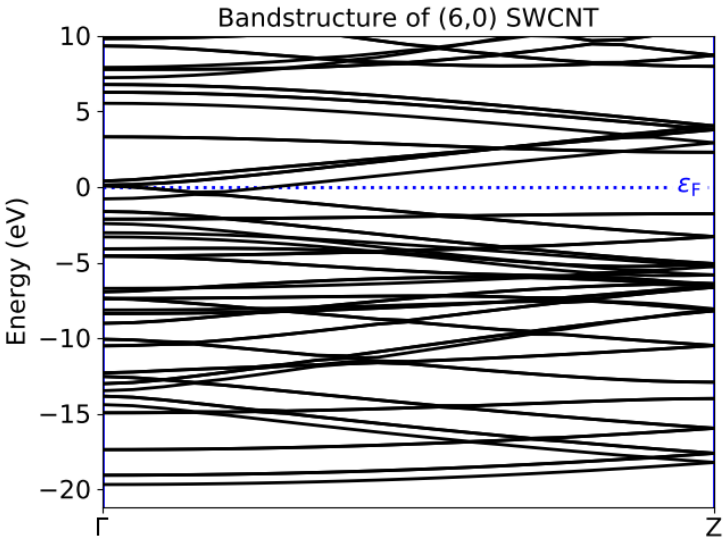

Fig. 7 First-principles calculated band structure for SWCNT with chirality (6,0)

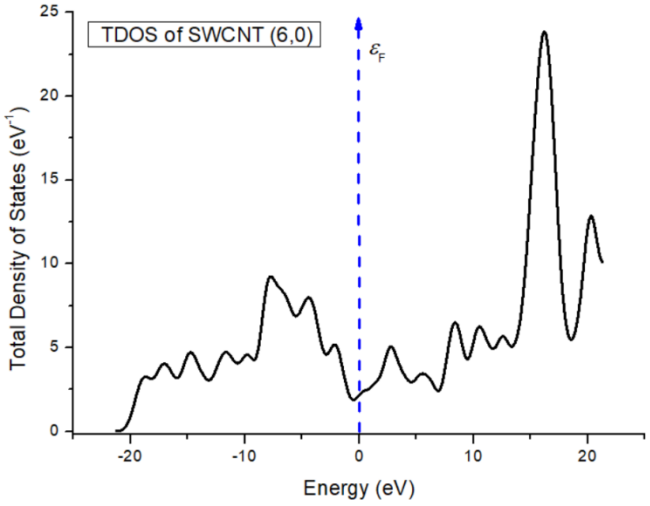

Fig. 8 First-principles calculated total density of states of SWCNT with chirality (6,0)

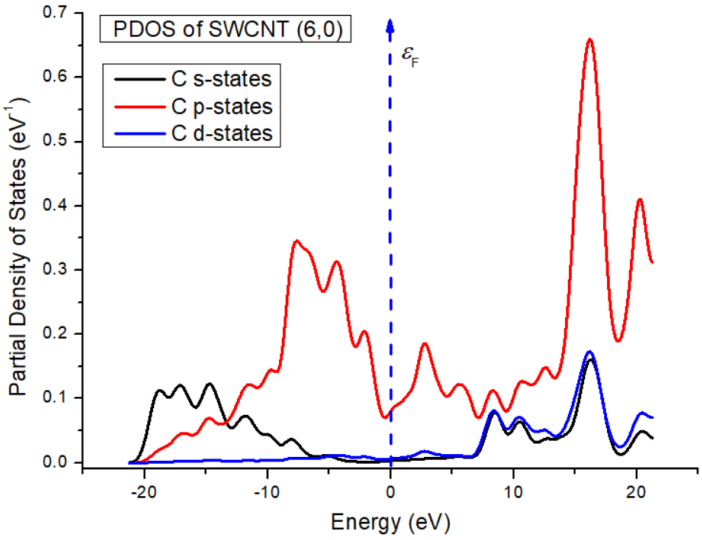

Fig. 9 First-principles calculated partial density of states of carbon in SWCNT with chirality (6,0)

C_{20} has a band gap of 0 eV in the study by [8] and C_{24} was reported with a range of 4.76 eV [7] and 4.89 eV [8]. From the first-principles results, we determined that all studied systems are direct band gap materials, where both the top of the valence band and the bottom of the conduction band are located at the center of the Brillouin zone (Γ-Γ transition). These findings are summarized in Table 1. The calculated electronic band structures, TDOS, and PDOS for SWCNT nanosystems with different chiralities (n=4-6; m=0) are shown in Figs. 2-9. In these figures, the Fermi energy level is set to zero electron volts, as indicated by the dotted lines. We observed that certain energy levels in the computed electronic band structures cross the Fermi energy, indicating that the SWCNT systems with chiralities (n=4, 5, 6; m=0) exhibit metallic behavior with a 0 eV band gap. This result is consistent with the findings reported in Refs. [7, 8]. Additionally, another study [11] suggests that for nanotubes with small diameters, the curvature is sufficiently strong to induce rehybridization between the σ- and π-states, leading to band overlap and metallic behavior in SWCNTs. Our results align closely with those reported in Ref. [7]. A systematic analysis of the electronic properties of SWCNT systems reveals that the valence bands primarily consist of carbon s- and p-states, while the conduction bands are predominantly

derived from the p-states of carbon atoms.

3. Conclusion

In this study, we have investigated the electronic properties of single-walled carbon nanotubes (SWCNTs) with chiralities (n=4, 5, 6; m=0) using ab-initio modeling based on Density Functional Theory (DFT). Our results reveal that these SWCNT systems exhibit metallic behavior, characterized by a 0 eV band gap, consistent with prior studies [9, 10]. The analysis of the electronic band structures, total and partial density of states (TDOS and PDOS), indicates that the curvature of the nanotube surfaces plays a critical role in their electronic properties. For nanotubes with small diameters, the strong curvature induces rehybridization between the σ- and π-states, contributing to the metallic character observed in these systems, as noted in previous research.

Furthermore, our results suggest that the valence bands are primarily composed of carbon s- and p-states, while the conduction bands predominantly arise from the p-states of carbon atoms. These findings provide a deeper understanding of the chirality-dependent electronic properties of SWCNTs and underscore the importance of chirality in tuning the material's electronic behavior for potential applications in nanoelectronics, energy storage, and other advanced technologies.

The computational framework developed in this study can serve as a valuable tool for predicting the electronic characteristics of other SWCNT systems with varying chiralities, and could help guide the design of carbon-based nanomaterials for specific technological applications.

REFERENCE LIST

1. Barone, V., Peralta, J. E., Wert, M., Heyd, J., & Scuseria, G. E. (2005). Density functional theory study of optical transitions in semiconducting single-walled carbon nanotubes. *Nano Letters, 5*, 1621–1624.
2. Charlier, J. C., Blase, X., & Roche, S. (2007). Electronic and transport properties of nanotubes. *Reviews of Modern Physics, 79*, 677–732.
3. Domnin, A. V., Mikhailov, I. E., & Evarestov, R. A. (2023). DFT study of WS_2-based nanotubes electronic properties under torsion deformations. *Nanomaterials, 13*(19), 2699.
4. Khan, I. A., Afrooz, A. N., Flora, J. R., Schierz, P. A., Ferguson, P. L., Sabo-Attwood, T., & Saleh, N. B. (2013). Chirality affects aggregation kinetics of single-walled carbon nanotubes. *Environmental Science & Technology, 47*(4), 1844–1852.
5. Liu, B., Wu, F., Gui, H., Zheng, M., & Zhou, C. (2017). Chirality-controlled synthesis and applications of single-wall carbon nanotubes. *ACS Nano, 11*(1), 31–53.
6. Matsuda, Y., Tahir-Kheli, J., & Goddard, W. A. (2010). Definitive band gaps for single-wall carbon nanotubes. *The Journal of Physical Chemistry Letters, 1*, 2946–2950.
7. Monavari, S. M., & Memarian, N. (2023). Ab initio investigation for DNA nucleotide bases sequencing using chiral carbon nanobelts and nanotubes. *Scientific Reports, 13*(1), 18063.
8. Orazi, V., Ambrusi, R. E., Morelli, A., Juan, A., & Marchetti, J. M. (2024). DFT study of the stability and electronic properties of Ni-doped defected (6,0) and (8,0) single-walled carbon nanotubes. *Materials, 17*, 6236.
9. Ouyang, M. (2001). Energy gaps in "metallic" single-walled carbon nanotubes. *Science, 292*(5517), 702–705.
10. Slepchenkov, M. M., Barkov, P. V., Kolosov, D. A., & Glukhova, O. E. (2023). Ab initio study of optical properties of hybrid films based on bilayer graphene and single-walled carbon nanotubes. *C, 9*(2), 51.
11. Tans, S. J., Verschueren, A. R. M., & Dekker, C. (1998). Room-temperature transistor based on a single carbon nanotube. *Nature, 393*(6680), 49–52.

JOURNAL OF BAKU ENGINEERING UNIVERSITY - PHYSICS
2025. Volume 9, Number 1 *Pages 10-16*

UDC 538.951
DOI: https://doi.org/10.30546/09081.2025.001.8017

THE EFFECT OF NANOCARBON ON THE MECHANICAL PROPERTIES OF HIGH-PRESSURE POLYETHYLENE

M.A. MEHRABOVA*[1], A.N. HASANLI[2], E.R. BABAYEV[3], F.Sh. KERIMOV[1], S.İ. SAFAROVA[1], M.F. ASADOV[1]

[1]*Azerbaijan Technical University, Baku, Azerbaijan*
[2]*Azerbaijan University of Architecture and Construction Baku, Azerbaijan*
[3]*Department of Department of Science, Technical and Nanotechnology State Oil Company of Azerbaijan Republic, Baku, Azerbaijan*

Email:metanet.mehrabova@aztu.edu.az,aygul.hasanli7@gmail.com, elbey.babayev@socar.az,ferhad.kerimov@aztu.edu.az, seferova_sevinc@aztu.edu.az,musa.asadov1@gmail.com

ARTICLE INFO

Article history:
Received 2025-05-28
Received in revised form 2025-06-19
Accepted:2025-07-13
Available online

Keywords:
High-pressure polyethylene, UV radiation, nanocarbon, mechanical durability, polymer nanocomposites

ABSTRACT

New polymer nanocomposites based on high-pressure polyethylene grade 10803-020 and carbon nanotubes were developed, and the conditions for obtaining nanocomposites with optimal physical properties were determined. The primary goal of this work was to incorporate carbon nanotubes into polyethylene to produce nanocomposites with superior properties for construction applications. The composition and concentration of the nanoadditive which led to significant improvement in the electromechanical properties of high-pressure polyethylene were experimentally determined. Nanocarbon was used as a modifying additive. The developed nanocomposite is notable for the first-time introduction of a very small amount of nanocarbon into HPPE, varying within 0.01–0.1 mass %. It was found that including 0.05 mass % nanocarbon in high-pressure polyethylene significantly increases its mechanical strength.

The physicochemical changes in the resulting composite materials under electrical discharges in air and UV radiation were studied. It was shown that adding 0.05 mass % nanocarbon significantly enhances the material's resistance to electrical discharges and UV radiation. Considering the characteristics and technical parameters of high-pressure polyethylene + 0.05 mass % nanocarbon, this material can be widely used in various industries, including construction.

1.Introduction

Carbon nanotubes have been widely used in construction since the 1980s to strengthen structures in seismically active zones, such as California. They have proven effective in improving various materials, including reinforced concrete, metal, and stone [1]. Most commonly, carbon nanotubes are utilized to reinforce concrete structures. Durable surface layers for road pavements have been developed, using a "Carbon-polymer" binder. Structural panels

are employed in the construction of wall enclosures for low-rise buildings in cold climate regions. A distinguishing feature of these panels is the use of multi-layered insulating boards containing carbon. For enhanced thermal insulation with greater compression strength, carbon dioxide is used in the production process. Carbon particles are also added to professional-grade insulation boards used for roofing large areas such as shopping centers, industrial facilities, and residential complexes. Beyond construction, nanocarbon finds applications in other industries, including automotive, aviation, aerospace, sports equipment, medicine, and electronics [2–6]. Recently, carbon has started to influence interior design as well.

All the aforementioned data have led to the rapid growth of research into the physicochemical properties of nanoparticles and polymer composites based on them in recent decades [7]. Due to the small size of organic and inorganic nanoparticles, comparable to that of macromolecules, polymer nanocomposites exhibit unique electronic, photophysical, sensory, and other properties. Literature indicates the potential for significantly improving the physicomechanical properties of polymer compositions and materials through relatively small additions of nanodispersed powders [8]. The small size and surface properties of nanoparticles play a crucial role in determining their "compatibility" with the polymer matrix. Research efforts have focused on solving problems related to the distribution of carbon nanotubes (CNT) and enhancing the final properties of the composite. In [9], it was found that nanocomposites exhibit superior thermal stability compared to polyolefin materials, and it was demonstrated that the inclusion of nanotubes affects the crystalline behavior and structure of the polyethylene matrix. Studies [4–6] have explored the challenges faced by polyolefin-based composites in terms of manufacturing processes and industrial production of components for advanced engineering applications.

In [10-12], the study revealed that materials with carbon nanotubes possess exceptional qualities such as high strength, lightweight, corrosion resistance, and the ability to enhance structural rigidity and thermal conductivity. The use of nanofillers based on nanotechnology allows for the development of polymers that combine traditional and new qualitative characteristics, which may initially seem mutually exclusive. This is particularly beneficial in cases where it is necessary to simultaneously ensure transparency and flexibility, a certain degree of impact resistance and rigidity, as well as specific physical, insulating, and conductive properties.

The aim of this work is to develop a nanocomposite based on high-pressure polyethylene (HPPE) with nanocarbon additives to produce materials with enhanced mechanical and dielectric properties, improved thermal resistance, and reduced aging rate of the film during operation.

2. Methodology and Experimental

The study focused on HPPE grade 10803-020 as the base material, with carbon used as the additive. Carbon, represented by the symbol (C), manifests in various forms such as soft graphite and hard diamond [13] and disperses well in molten polymers. Additives of multi-layer carbon nanotubes in the range of 0.01–0.1 mass% were incorporated into the HPPE matrix via mechanical mixing in the molten state (table 1). For the production of films, a manual electrically heated hydraulic press (PG-60 model) was employed. The prepared HPPE – CNT mixture was loaded into a polished flat mold with a spacer thickness of 0.1 mm. To prevent adhesion, a fluoroplastic film (foil) was used. The mold was heated to 140–150°C and compressed under a pressure of 150 atm. After cooling, the films were extracted from the mold. The resulting films,

with a thickness of 60–80 μm, were used to prepare samples for the measurement of physical, mechanical, electrical, and optical properties.

Table 1. Characteristics of Multi-Layer Carbon Nanotubes

Indicator	**Physicochemical characteristics of** multi-layer CNT
1 Appearance	Black powder
2 Number of walls	8-9
3 Length	>100 mkm
4 Specific surface area	190 m^2/q
5 Average diameter	12-13 nm
6 Bulk density	0,056 kg/dm^3
7 Purity, at least	85 %

The uniformity of the films was assessed by measuring their thickness across the entire surface. Film thickness was determined using an optical thickness gauge (N3B-2) and a micrometer. The thickness value of each sample represents the arithmetic mean of 10 measurements.

UV irradiation was provided by the DRSH-500 light source. The main components of the light source are a spherical mercury-quartz lamp of high pressure (type DRSH-500) and a semi-spherical reflector (fig.1). The DRSH-500 mercury-quartz lamp is a powerful, concentrated radiation source in the visible and ultraviolet parts of the spectrum. The lamp operates in a confined space (housing) under conditions where the housing size and ventilation are such that the air temperature at a distance of 60 mm from the walls does not exceed 250°C.

A sample with a thickness of 50 μm, supported by an duralumin frame using a holder, is mounted on a stand. UV rays are directed towards the center of the melt. The distance from the source to the sample is 250 mm. The distance of 250–200 mm enhances the effect of UV irradiation (aging).

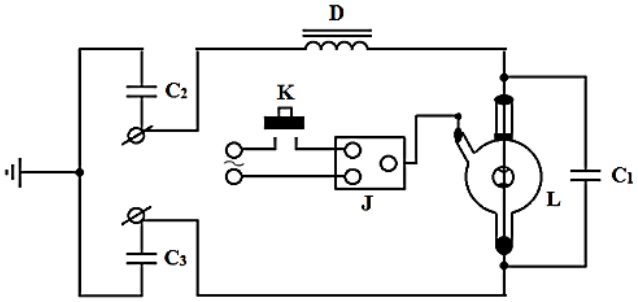

Figure.1. Ignition block for the DRSH-500 lamp: D – ballast; L – lamp; K – end switch;
J – ignition inductor with spark length of 15-20 mm; C1 – capacitor for shunting the lamp with a capacitance of 0.05 μF, rated for at least 250V; C2, C3 – capacitors with capacitance of 0.5 μF for grounding the network, with a rated voltage of at least 250V. Calibration of the effective UV radiation is attempted every 300 hours.

UV rays hit the sample at a right angle. The experiment was conducted at room temperature (20°C). The experimental procedure is as follows: the lamp is clamped using an inductor with a spark length of 15-20 mm. The nominal voltage on the lamp is 70V, with a current of 7.5A. This generates a nominal light flux of 22,500 lm. The sample was irradiated for 15 and 30 hours.

Measurement of mechanical durability σ, i.e. the time elapsed from the moment of sample loading to its fracture, at different load values in the test cell, is shown in fig. 2.

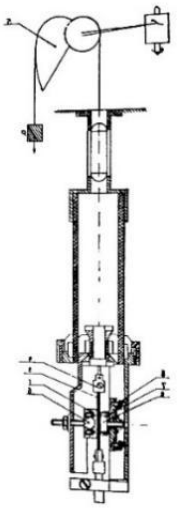

Figure. 2. Setup for determining the mechanical strength of polymer film materials: 1, 2 - electrodes; 3 - sample; 4 - clamps; 5 - lever mechanism; 6 - ball; 7 - safety ring; 8 - springs.

3. Results and discussions

In fig.3, the graphs show the dependence of the logarithm of the durability time $\lg\tau_\sigma$ on the mechanical stress of the HPPE film without additives and the influence of CNT additives containing 0.01-0.1 mass%. As can be seen from fig. 3, the time dependence of the strength is characteristic for all the investigated materials, and the relationship between durability and stress follows an exponential law:

$$\tau = Ae^{-\alpha\sigma} \qquad (1)$$

here A is the coefficient, α is the structurally sensitive coefficient, which depend on the nature of the material being studied and the test temperature [14].

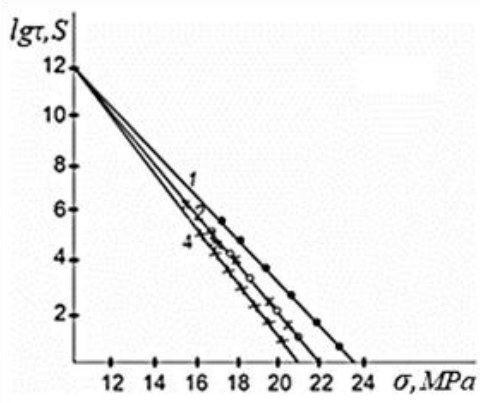

Figure.3. Stress dependence of the mechanical durability of HPPE film (initial) and its modifications: 1 - HPPE + 0.05 mass% CNT, 2 - HPPE (initial), 3 - HPPE + 0.03 mass% CNT, 4 - HPPE + 0.1 mass% CNT.

From fig.3, it is evident that the introduction of a small amount of CNT into HPPE leads to an increase in its mechanical strength, i.e., an improvement in the strength properties of HPPE when 0.05 mass% CNT is added (line 1) compared to HPPE without additives (line 2) and HPPE + 0.03 mass% (line 3). As the CNT content increases further (up to 0.1 mass%), a sharp decrease in the material's mechanical strength is observed (line 4).

Based on the experimental results, it can be concluded that the observed increase in the strength properties of HPPE when 0.05 mass% CNT is added is related to a change in the coefficient α, as α—the structural coefficient—depends not only on the nature of the material but also on its structure.

As follows from the obtained experimental results, the introduction of the optimal content of the proposed CNT additive into HPPE leads to an increase in mechanical strength by more than 15%. The optimal concentration of the additive depends on the specific application area of the polymer matrix. Therefore, when using organic and inorganic additives, it is recommended to determine the optimal concentration through tests with several different concentrations. After multiple experimental studies of the physico-mechanical properties, the effectiveness of adding 0.05 mass% CNT was proven.

It is known that the linear dependence of lgτ on σ is valid at different temperatures. Through prolonged mechanical testing of the material, the temperature-time dependence of the material's mechanical strength was determined.

For practical purposes, the most significant interest lies in determining the mechanical durability at different temperatures. To verify this, the durability dependence on mechanical stress was studied in the temperature range of 223 - 138 K for HPPE films and their optimal modification.

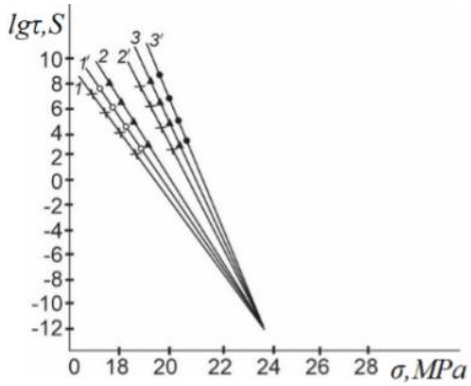

Figure.4. Strength dependence of the durability of HPPE film (1-3) and its optimal modification (1'-3') at different temperatures.

1, 2' - 173 K; 2 - 153 K; 3, 3' - 138 K; 1' - 223 K

It follows from fig. 4 that for all films in the investigated temperature range, the well-known durability equation (1) is satisfied at a constant temperature. According to experimental studies, when the optimal amount of additives (HPPE + 0.05 mass% CNT) is introduced, there is an increase in its mechanical strength (line 1') and a slight decrease in the lifetime at different temperatures (lines 2', 3'), whereas for the CNT -free film, a decrease in strength is observed (1, 2, and 3).

The change in mechanical strength of HPPE and its optimal modification as a function of temperature is depicted by a fan-shaped family of lines, which, when extrapolated, converge at one point – the pole, at a durability value of $\tau_\sigma = 10^{-2}$s.

The increase in the mechanical strength of HPPE at the optimal content (0.05 mass% CNT) is likely related to structural changes occurring after the addition of the additives [15].

Considering the key characteristics and technical parameters, HPPE can be widely used in various industries: from packaging and pipelines to automotive and construction.

The physicomechanical characteristics of HPPE are sensitive to the introduction of nanocarbon additives. A content of 0.05 mass% nanocarbon is optimal as it provides the greatest resistance to mechanical stresses and UV radiation compared to both the original HPPE and HPPE with other additive concentrations.

The introduction of the proposed nanocarbon additive in the specified amount into HPPE prevents processes leading to its electrical aging and UV radiation, thereby enhancing its physicomechanical properties within this temperature range.

Based on this, we have studied the effect of nanocarbon in the optimal amount on the change in mechanical strength under UV radiation in air. The obtained experimental data are presented in fig. 5.

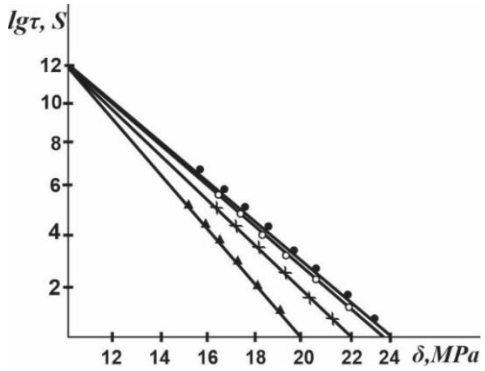

Figure. 5. Strength dependencies of the mechanical durability of the HPPE film and its modification before and after UV radiation in air: 1,2 - HPPE + 0.05 mass% CNT before and after UV radiation; 3,4 - HPPE (original) before and after UV radiation, t_{ob}=15 hours.

From fig. 5, it can be seen that UV radiation on HPPE films without any additives leads to a noticeable decrease in its mechanical strength (lifetime) (line 4). However, under the same conditions, the introduction of the proposed nanocarbon into HPPE, in the optimal amount, contributes to the stability of its modified mechanical properties.

Indeed, when evaluating the data from Figure 4, it becomes evident that the introduction of nanocarbon into HPPE in the optimal amount results in enhanced properties, with the modified HPPE remaining unchanged (line 2) after UV radiation exposure for 15 hours in air. The observed increase in mechanical strength and stability of the HPPE modification can be attributed to the structuring features of the specified additive, which ensures the dense packing of macromolecules during the film formation process.

4. Conclusion

The effect of a small amount of nanocarbon on the mechanical strength of HPPE was studied. Through experimentation, the possibility of obtaining a nanocomposite with physical and mechanical properties based on HPPE grade 103-03-020, with added CNT, was established. The range of filler content was experimentally determined, i.e., the optimal composition of the studied nanocomposite was identified to improve operational characteristics. The developed nanocomposite of HPPE is distinguished by the fact that for the first time, a significant small amount of CNT additives was introduced into the composition of HPPE, varying from 0.01 to 0.1 mass %. It was found that increasing the CNT content in HPPE significantly reduces its mechanical strength, with a positive effect observed only at 0.05 mass% of the additive. It was established that the developed HPPE nanocomposite has relatively enhanced resistance to

electrical and UV radiation exposure. The effect of CNT on the mechanical strength of HPPE at different temperatures was studied. It was determined that CNT in small amounts (0.05 mass%) significantly increases the mechanical strength at various temperatures.

REFERENCES

1. Sokolova V.V., Yudin A.A., Islamgalieva D.R., Nurislamova R.K. (2022). Benefits of carbon fiber and ways of application// The Eurasian Scientific Journal, 14(3): 46SAVN322. Available at: https://esj.today/PDF/46SAVN322.pdf.
2. Ibrahimov B. G., Hashimov E. Q., Hasanov A. H., Talıbov A. M. (2022). Research and analysis indicators fiber-optic communication lines using spectral technologies// Advanced Information Systems. 6(1), 61-64, https://doi.org/10.20998/2522-9052.2022.1.10
3. Ibrahimov B. G. (2023). Investigation of Noise Immunity telecommunication systems according to the criterion energy efficiency //Transport and Telecommunication. 24 (4), 375 – 384, DOI 10.2478/TTJ-2023-0029
4. Hasanli A.N., Mehrabova M. A. (2024a).. Smart Technology for Security in Tourism Complexes// Engineering World. 6, 240-245, DOI:10.37394/232025.2024.6.26
5. Hasanli A. N., Mehrabova M. A. (2021b). The Influence of Alternative Energy Means on the Architectural Shaping // International Journal of Cultural Heritage. 6, 26-30, https://iaras.org/iaras/filedownloads /ijch/2021/017-0004(2021).pdf
6. Nuriyev I. R., Mehrabova M. A, Nazarov A. M, Hasanov N. H., R. M. Sadigov, Farzaliyev S. S., Farajov N.V. (2019). Structure and Surface Morphology of $Cd_{1-x}(Mn,Fe)_xSe$ epitaxial films // Journal of Surface Investigation: X-ray, Synchrotron and Neutron Techniques. 13, 1083-1085, https://doi.org/10.1134/S1027451019060168
7. Kim S. (2014). Raw Materials-Composites-Carbon Fiber The Chemical Journal. // 10, 64–73. https://tcj.ru/wp-content/uploads/2014/11/ 2014_10_63-73_PLAST-Syre.pdf
8. Korenets A. M., Bratoshevskaya V. V. (2021). Use of carbon fiber in modern construction Scientific support for the agro-industrial complex // Collection of articles based on the materials ofthe 76th scientific and practical conference of students on the results of R&D for 2020. Krasnodar. 99-100, https://naukaip.ru/wp-content/uploads/2022/02/%D0%9 C%D0% 9A-1319. pdf
9. Zeynalov Sh. A. , Kerimov F. Sh., Safarova S. İ., Sadygova S. H., Musaev T. P. (2023). Influence of the phthalimide on the process of electrical aging of the high-pressure polyethylene // Scientific Herald of Uzhhorod University. Series "Physics". 54, 18-26 https://doi.org/10.54919/physics/54.2023.18
10. Chenchen Wu, Fan Xu, Huixiong Wang, Hong Liu, Feng Yan, Chao Ma. (2023). Manufacturing Technologies of Polymer Composites—A Review // Polymers. 15(3), 712, https://doi.org/10.3390/polym15030712
11. Magerramov A. M., Shukyurova A. A., Nuriev M. A. (2018). Electrical Conductivity of Nanocomposites Based on Low-DensityPolyethylene and Cu_2S Nanoparticles // Surface Engineering and Applied Electrochemistry, 54(1),32–37. https://link.springer.com/article/10.3103/S1068375518010118
12. Mehrabova M. A., Mammadova S. I., Kerimov F. Sh., Safarova S. I., Gulmamedov K. J.,Hamdillayeva İ.H. (2024). Influence of Discharges and UV Irradiation on the Electrical Properties of High Pressure Polyethylene and Compositions on Its Base // Polymer-Plastics Technology and Materials. 63(16), 2237-2245, https://doi.org/10.1080/25740881.2024.2369677
13. Kelly A. (2009). Engineering triumph of carbon fibers // Composites and nanostructures. 1,38-49, http://www.issp.ac.ru /journal/composites/2009/2009_1/ kelly.pdf
14. Slutsker A. I. (2008).Effect of mechanical loading on the kinetics of electrical destruction of polymers // Journal of Technical Physics, 78 (11), 57-62 https://journals.ioffe.ru/articles/viewPDF/9542
15. Paszkiewicz S., Szymczyk A., Zubkiewicz A., Subocz J., Szczepaniak J. (2020). Enhanced Functional Properties of Low-Density Polyethylene Nanocomposites Containing Hybrid Fillers of Multi-Walled Carbon Nanotubes and Nano Carbon Black // Polymers (Basel), 12(6), 1356, https://doi.org/10.3390/polym12061356

JOURNAL OF BAKU ENGINEERING UNIVERSITY - PHYSICS
2025. Volume 9, Number 1 *Pages 17-21*

UDC 621.315.592.541.65
DOI: https://doi.org/10.30546/09081.2025.001.8008

BAND STRUCTURE OF $TlInSe_2$ AND $InGaTe_2$ TRIPLE COMPOUNDS

U.S. ABDURAHMANOVA

Baku Engineering University,

Bakı, Azerbaijan

E-mail: uabdurahmanova@beu.edu.az

ARTICLE INFO

Article history
Received:2025-09-18
Received in revised form:2025-07-04
Accepted:2025-07-14
Available online

Keywords:
triple compounds, tetragonal syngony, band structure, semiconductors.

ABSTRACT

In this research work we present the results of calculations of energy spectra and band structure of $TlInSe_2$ and $InGaTe_2$ triple compounds crystallized in the tetragonal syngony. For calculations we used pseudopotential method and functional density theory in the approximation of the combined gradient using LAPW method and WIEN 2K program code. Some properties of these compounds are determined based on their band structure. It is known that search for new semiconductor materials is usually carried out in the direction of expansion of the group of crystal structure of already known materials. In particular, study of crystal structure of TlSe showed that this phase is distinguished by extreme specific features. TlSe lattice turns out to be composed of two independent structural units - from octahedron with ionic bond Tl^{+}- Se and tetrahedron with covalent bond between Tl^{3+}-Se and therefore chemical formula of TlSe should be written as $Tl^{+}Tl^{+3}Se_2$. Thus, by replacing the trivalent thallium atom with corresponding trivalent atoms, in particular, gallium and indium, in the TlSe lattice, a new class of semiconductor compounds of the $A^{III}B^{III}C_2^{VI}$ type was obtained.

1. Introduction

The great interest in type $A^{III}B^{III}C_2^{VI}$ compounds is that they do not have pairs of valence electrons, the chemical bond is strongly asymmetric, the crystal structure has special features, and the chemical composition is managed within a certain crystal structure.

The crystal structures, electrophysical, thermal-physical, optical and photoelectric properties of the mentioned type crystals have been studied and the research in this direction is systematically continued [1- 3].

By studying the possibilities of applying these compounds, it was determined that compound $TlInSe_2$, which is a typical representative of the mentioned compounds, has high sensitivity in the visible and near- infrared parts of the spectrum, memory switching properties, and tenso sensitivity. It was determined that $TlInTe_2$ and $TlGaTe_2$ compounds which are structural analogues of this group, have high tenso-sensitivity and memory switching properties.

Triple semiconductor compounds are characterized by their specific characteristics. $TlSe$ -type crystals also have the possibility of wide application in semiconductor tensometry. Compound $TlInSe_2$ is particularly promising in this regard. It has very high strain sensitivity, which can be increased and controlled depending on temperature, deformation, and the effect of electromagnetic waves.

X-ray structural studies have shown that some of the triple semiconductor compounds of $A^{III}B^{III}C_2^{VI}$ type have a chain structure, while the others have a layered structure [4]. The results of X-ray phase analysis showed that solid solutions based on compounds $TlInSe_2$ and $InGaTe_2$ crystallize in the tetragonal syngony [5]. The change of lattice constants of $TlInSe_2$ in the solubility regions depending on the composition mainly obeys Vegard's law.

The calculation of the energy spectrum using modern methods and programs, system analysis, identification of the results of compounds of the $A^{III}B^{III}C_2^{VI}$ type having a chain crystal structure have not been carried out before. Some properties, obtaining methods, growing technologies of the monocrystals of these type compounds have been determined [7-10].

In this work the results of calculation of energy spectra of $TlInSe_2$ and $InGaTe_2$ compounds are presented.

Results of the studies of $TlInSe_2$ compound show that, the upper level of the valence band of this compound is at the T_1 point and the lower level of the conduction band is located at the border of the Brullien zone of the volume-centered tetragonal lattice. However, indirect transitions are possible in this compound. Direct transition is not possible according to the selection rule. From these calculations, the following values were obtained for direct and indirect transitions in $TlInSe_2$: $\Delta E(indirect) = 1{,}21eV$ and $\Delta E(direct) = 1{,}3eV$ (figure 1).

The valence band can be divided into three groups depending on their composition and nature [12-14].

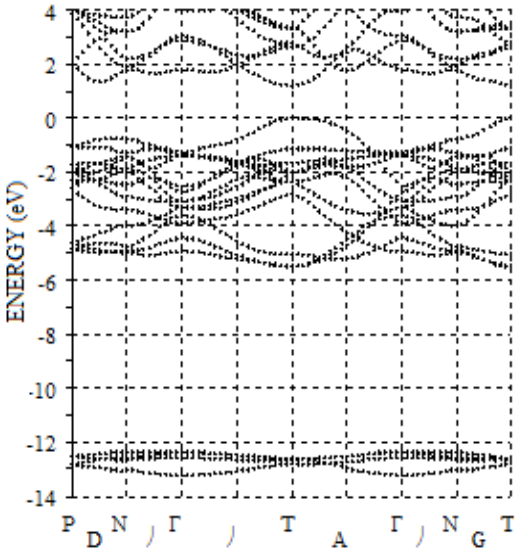

Figure1. Band structure of $TlInSe_2$

The energy spectrum of $TlInSe_2$ was calculated using the pseudopotential method. It was found that the top of the valence band is located at the highly symmetric point T on the surface of the Brillouin zone and the irreducible image corresponds to T3, and the bottom of the conduction band is located on the line D in the middle between the points P (π/α, π/α, π/c) and N (π/α, π/α,0), corresponding to the irreducible representation D1.

The transition with the lowest energy occurs between the states T3 and T4 and is forbidden in the dipole approximation. The width of the forbidden band obtained from calculations is about 1 eV. The valence band can be conditionally divided into three groups:

- The lowest group with four bands near -12.6 eV owes its origin to the 4s-states of Se.
- Another group of four bands in the region of –(4÷5.5) eV is associated mainly with the 6s-state of Tl atoms and the 5s-state of In.
- The upper group of ten bands in the region of (0÷3.5) eV is formed mainly by the 4p-state of Se atoms, the 6p-state of Tl atoms and the 5p-state of In atoms.

The data on the origin of the bands agree with the results of work, in which the photoemission spectra were studied and the band structure of $TlInSe_2$ was calculated using the plane wave addition method.

The theoretical conclusion of the work, which showed the presence of an isolated group consisting of two zones of the upper part of the valence band of the semiconductor compound $TlInSe_2$, was not confirmed in this work and in the work. Probably, this is due to the incorrect consideration of the screening of pseudopotentials inherent in the empirical method.

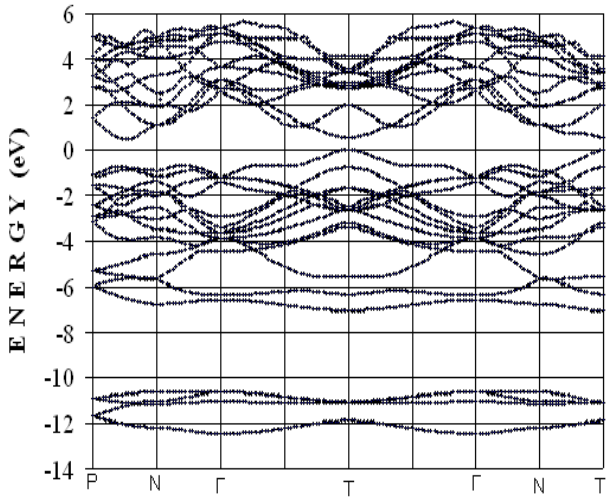

Figure 2. Band structure of $InGaTe_2$

The calculation of the electron spectrum of $InGaTe_2$ was carried out at the symmetric points G, T, N, P and along the lines connecting these points. The results of the calculation of the band structure are presented in figure 2. The valence band of $InGaTe_2$ consists of three subbands.

The lower group, consists of four bands, is separated from the others by a wide energy gap of ~6 eV. The group-theoretical analysis shows that these lower valence bands, located near -10÷11eV, owe their origin to the 5s- state of Te.

The next group of tetravalent bands, located at the energy level of about -5 eV, arises mainly from the *s*-states of In and Ga atoms.

The third large group of ten bands with a width of 5 eV is due to the *p*-states of In, Ga and Te atoms.

According to conducted calculations, the band gap is determined as 0.56 eV.

2. Methodology

The pseudopotential method is one of the main methods for calculating the energy spectrum of charge carriers in semiconductors [6,15]. The energy spectrum of $TlInSe_2$ one of the base samples

of $A^{III}B^{III}C_2^{VI}$ types of compounds, was calculated using the pseudopotential method. At this time, the analytical expression proposed by Konstantinov and others was used for atomic pseudopotentials. The form factors of ion potentials proposed by them consisted of 4 parameters

The idea of the pseudopotential method is first encountered in the work of Philips. In their work, Phillips and Kleinman developed the pseudopotential method and gave it a more rigorous formulation. In all cases, the pseudopotential theory is based on three fundamental physical approximations.

1. The first approximation is the self-consistent field approximation. In this approximation, the interaction between electrons is described by some average potential, which itself depends on the states of the electrons, and the electron states are in turn determined by the average potential.

2. In the second approximation, all electron states are divided into inner shells and conduction band states, and it is assumed that the wave functions of the inner shells are strongly localized.

3. The third fundamental approximation is the use of perturbation theory for electrons in the conduction band.

The electronic band structure of the $InGaTe_2$ crystal was determined at the symmetric points and lines of the Brillouin zone of the $InGaTe_2$ crystal using the LAPW method in the Density Functional Theory approximation and the WIEN2k software package and the results were analyzed. The Generalized Gradient Approximation (GGA) was used as the exchange-correlation potential.

For this purpose, the lattice parameters and atomic coordinates were first determined from first principles (ab-initio) by minimizing the energy and Hellman–Feynman forces.

To calculate the band structure of $InGaTe_2$, the optimized values of the lattice parameters a=8.3945 Å; c=6.8352 Å and the chalcogen parameter x=0.1730 were taken.

3. Conclusion

The band structure of $TlInSe_2$ compound was studied using the pseudopotential method, and the band structure of $InGaTe_2$ compound was studied using density functional theory. As a result of the studies, it was determined that, the valence band can be divided into three subgroups.

The valence band can be conditionally divided into three groups:

The lowest group with four bands near -12.6 eV is formed from the *4s*-states of Se, the next group of four bands (4÷5.5 eV) is releated to the *6s*-state of Tl and the *5s*-state of In atoms. The upper group of ten bands in the region of 0÷3.5 eV is formed by the *4p*-state of Se atoms, the *6p*-state of Tl atoms and the *5p*-state of In atoms.

Studies of the band structure of the $InGaTe_2$ compound represent that it was calculated using density functional theory and the valence band of the $InGaTe_2$ compound consists of three groups. The lowest group consists of 4 bands located at a distance of ~ 6 eV from the others. Theoretical-group analysis shows that these bands, located around –11 eV÷–10 eV, arise from the 5s states of tellurium atoms, the next group of 4 bands is located at the –5 eV level and arises from the *s*– states of indium and gallium atoms. The group of 10 bands with a width of 5 eV arises from the *p*– states of In, Ga and Te atoms.

REFERENCES

1. Müller D., Eulenberger G., Hahn H. (1997) Uber Tirnare Thallium-Chalkogenide Mitthalliumselenide Structures // Z. anorg. allg. Chemie, V. 398, №2, p. 207-220.
2. Mobarak M., Berger H., Lorusso G.F. et al. (1998). The Growth and Properties of Single Crystals of $GaInTe_2$, a Ternary Chalkogenide Semiconductor // J.Physics D: Appl. Physics, V. 31, №12, p. 1433-1437.
3. Gashimzade F.M., Orujov G.S. (1980). Calculation of the energy spectrum of electrons of ternary semiconductor compounds with the structure of thallium selenide // Azerb. USSR, v. 36, №12, p. 18-23.
4. Guseinov G.D., Mooser E., Kerimova E.M. et al. (1969). On some properties of $TlInS_2$(Se_2, Te_2) syngle crystals // Phys. Stat. Sol., v.34, p.33-44
5. Gojaev E.M., Jafarova S.R., Gulmammadov K.D., Mammadov E.M., Osmanova S.S., (2009). Synthesis and growth of TlInSe2 and TlGaSe2 single crystals // Inorganic materials, v. 45, №7, p.790-792.
6. Xeyne V., Koen M.L., Ueyr D., (1973). Pseudopotential theory, Moscow, «Mir», 557 pp.
7. Gojaev E.M, Orujov G.S., Kerimova R.A., and etc. (2006). Band structure and optical properties of the chain compound $TlInTe_2$ // Solid State Physics, v.48, № 1, p.40-43.
8. Abdurahmanova U.S., (2022). Synthesis and photoconductivity of crystal $InGaTe_2$ Journal of Physics, Baku Engineering University, Baku, Azerbaijan, ISSN 2521-6368, vol 6, No2, p. 72-77.
9. Orudzhev G., Mamedov N., Uchici H. et al. (2003) Band Structure and Optical Function of TernaryChain $TlInSe_2$ // J. Phys. Chem. Solids. V. 64. P. 1703.
10. Gonze X., Beuken J.M., Caracas R. et al. (2002) First_Principles Computation of Material Properties: the ABINIT Software Project // Allan. Comput. Mater. Sci. V. 25. P. 478–492.
11. Gojaev E.M, Jafarova Q.S., Safarova S.I., (2013), Band structure of TlInTe2 and thermal efficiency of solid solutions based on it // Thermoelectricity. № 1. p. 28–33.
12. Lencer D., Salinga M., Wuttig M. (2011) Design Rules for Phase change Materials in Data Storage Application // Adv. Mater. T. 23. № 18. C. 2030–2058.
13. Vinoqradov E.A., hasanli H.M., Javadov B.M., Tahirov V.I., (1979) Infrared reflection spectra of layered single crystals TlGaTe2, TlInTe2 and TlInSe2//SSP. v. 21. № 9. p. 2793–2796.
14. Navikova S.I., (1972), "Solid State Physics and Thermodynamics", Novosibirsk, p.56
15. Bachelet, G.B., Haman D.R., Shlüter V., (1982), Psevdopotensials that work: from H to Pu//Physical Review B, 26, N 8, 4199-4228

JOURNAL OF BAKU ENGINEERING UNIVERSITY - PHYSICS
2025. Volume 9, Number 1 *Pages 22-28*

UDC:539.23:535.34:535.37
DOI: https://doi.org/10.30546/09081.2025.001.8029

TUNING THE STRUCTURE, OPTICAL AND PHOTOLUMINESCENCE PROPERTIES OF POLYVINYLIDENE FLUORIDE AND CdS/ZnS-based NANOCOMPOSITES

Gullar SAFARALIYEVA, Flora HAJIYEVA*, Maarif JAFAROV

Baku State University,
Baku, Azerbaijan, Zahid Khalilov street 23

ARTICLE INFO

Article history
Received:2025-06-13
Received in revised form:2025-06-19
Accepted:2025-10-03
Available online

Keywords:
Nanoparticles; Nanocomposites; Photoluminescence; Polyvinylidenefluoride; Polymer

ABSTRACT

Have been developed a hybrid nanomaterials for applications in solar cells. Using ultraviolet spectroscopy, the optical absorption edges of the polymer nanocomposites have been determined, establishing that as the concentration of nanoparticles in the polyvinylidene fluoride matrix increases, the band gap decreases. Scanning electron microscope and X-diffraction analysis indicate that the cadmium and zinc sulphide nanoparticles are distributed in the polyvinylidene fluoride polymer as a separate phase and do not form a solid solution within the polymer matrix. Photoluminescence analysis reveals that for polymer nanocomposites with a hybrid combination of quantum dots, luminescence is observed over a wide range of wavelengths.

1. Introduction

The study of semiconductor quantum dots (QDs) of AIIBVI type has drawn a great deal of attention due to the widespread use of these materials. Already today, these nanoparticles and the composites based on them are used to create a new generation of LEDs, including white light sources with a very high (up to 90) color rendering index (CRI), as highly efficient luminescent bio labels, as well as active media for laser generation. Semiconductor nanoparticles possess several unique properties and successfully compete with traditional organic dyes. They have a higher molar extinction coefficient than dyes and a much higher photostability that is retained at excitation power densities up to 10^6 W/cm^2. One of the most vividly manifested trends in recent years is the use of polymers as a matrix for NPs since the nature of these polymers- the chemistry of functional groups, their structure allows regulating the production of the composite. An important point is that the polymers not only serve as a medium for dispersing NPs and facilitating the processing of the material as a whole, but can also contribute, leading to the synergism of the properties of the components. In particular, we are talking about both a possible increase in the filling limits of the material with NPs without their uncontrolled aggregation and the optimization of the optical properties of materials containing NPs. The optical properties of such materials serve as the basis for such current and future practical applications as optical absorption in a wide spectral range and photoluminescence (PL).

Recently, interest has increased in hybrid polymer nanocomposites, where several quantum dots are introduced into an optically transparent polymer matrix simultaneously. This is because such materials lead to an improvement in the efficiency of solar energy conversion by solar cells due to the creation of luminescent layers on their surface. Such hybrid layers based on QDs can convert UV radiation to a longer wavelength region, which is optimal for widely used solar cells. In this case, layers based on quantum dots can, in principle, divide the solar spectrum into

several spectral bands, optimized for various types of photocells. Surface luminescent layers for solar cells must have a transparent matrix that is optimal for the introduction of quantum dots into it, which in turn must have absorption bands in the UV region, the required red shift of the luminescence, a high quantum yield, and stable characteristics. Among semiconductor nanoparticles, ZnS and CdS are of huge interest because of their different optoelectronic applications. Quantum dots based on CdS and ZnS, which have weak degradation and the ability to select absorption and luminescence characteristics by varying their sizes, are very promising. A combination of materials from different kinds of semiconductor nanoparticles shows very distinctive properties that have never been observed in composite systems consisting of only one of the types of semiconductors [1-5].

In the literature analysis, the synthesis and characterization of polymer nanocomposites based on hybrid quantum dots have been rarely studied. Therefore, the purpose of this article is to study hybrid nanomaterials based on an optically transparent PVDF polymer and nanoparticles of cadmium and zinc sulfides.

2. Experimental part

Materials:

All chemical reagents were used without preliminary purification: polyvinylidene fluoride (PVDF, Solvay 6020/1001), cadmium chloride ($CdCl_2 \times 5H_2O$, Sigma Aldrich C3141), sodium sulfide (Na_2Sx9H_2O, PLC 141687), CTABr (cetyltrimethylammonium bromide % chemically pure), zinc chloride ($ZnCl_2$, PLC 141779), dimethylformamide (DaejungCAS No. 68-12-2).

Synthesis of polymer nanocomposites:

CdS and ZnS nanoparticles were synthesized and stabilized in the presence of the surface-active substance CTABr according to the works [6]. Polymer nanocomposite materials were synthesized using solution casting method. PVDF polymer was dissolved in dimethylformamide at a room temperature. Nanopowders of CdS and ZnS were added into PVDF solution at 1, 3, 5, and 10% contents and stirred until a homogeneous mixture was prepared. The solution was dried in air until the DMF solvent completely evaporated. To completely remove the solvent from the volume of the PVDF, the films were dried in a vacuum oven for a hour. Then, using hot pressing method at the melting temperature of polymer (180^0C) thin nanocomposite films were obtained.

Characterization of nanocomposites:

XRD analysis was performed on a diffractometer Rigaku Mini Flex 600 equipped with Cu K α radiation at room temperature. The structure of the nanocompositions was studied using Integra-Prima atomic force microscopy (AFM, NT-MDT, Zelenograd) and scanning electron microscopy (SEM, Jeol JSM-7600 F). The photoluminescence properties of nanomaterials were studied using a Varian CaryEclipse spectrofluorimeter. UV analysis have been realized using spectrophotometer Specord 250 Plus.

3. Results and discussion:

Figure 1 shows the diffraction patterns of PVDF+CdS/ZnS-based nanocomposites depending on the content of CdS and ZnS nanoparticles in the PVDF matrix. As seen from XRD patterns with the introduction of CdS and ZnS nanoparticles into the matrix, the intensity of the peaks belonging to the α-phase of PVDF polymer (18.83°; $26,8^0$; 35.43° and 41.19°) and for the β-phase

(20.6^0) decreases. It was also found that an increase in the content of nanoparticles, appearing peaks characterize both CdS and ZnS nanoparticles with the wurtzite crystal structure. While peaks at 24.9^0 (002) and 43.9^0 (103) belong to cadmium sulfide nanoparticles, peaks at 30.5^0 (101) and 51.5^0 (103) correspond to zinc sulfide nanoparticles in the diffraction pattern of PVDF+5%CdS/ZnS nanocomposite [7,8].

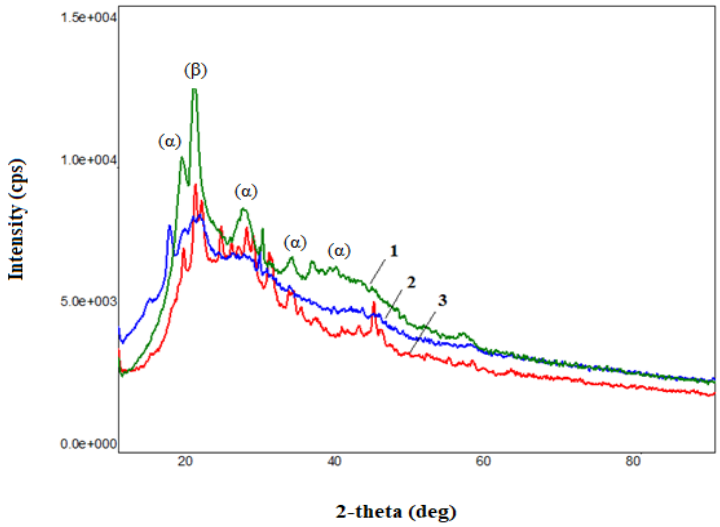

Fig.1 XRD patterns of PVDF+CdS/ZnS based nanocomposites: 1.PVDF+1%CdS/ZnS; 2.PVDF+3%CdS/ZnS; 3.PVDF+5%CdS/ZnS.

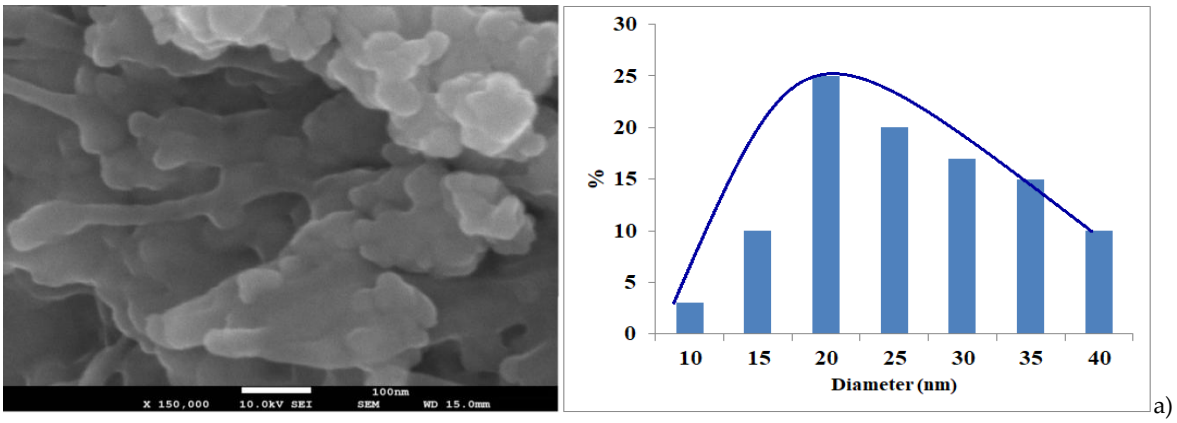

a)

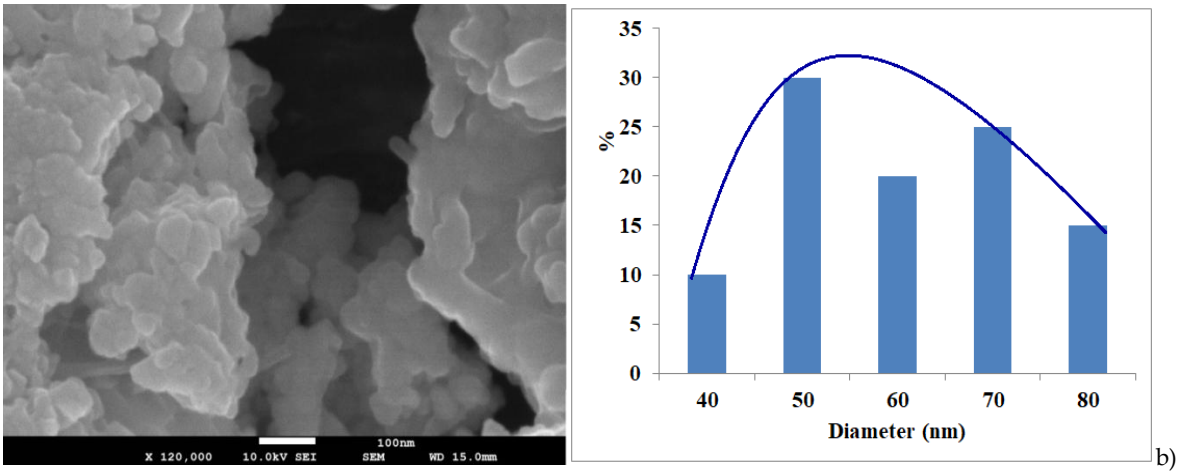

b)

Fig. 2 SEM images and particle size distribution of CdS and ZnS nanoparticles in PVDF matrix: a) PVDF+1%CdS/ZnS; b) PVDF+10%CdS/ZnS.

Figure 2 shows SEM images and particle size distribution of CdS and ZnS nanoparticles in PVDF matrix for PVDF+1%CdS/ZnS and PVDF+10%CdS/ZnS nanocomposite. According to SEM images, CdS and ZnS nanoparticles are uniformly distributed and the nanoparticle size for PVDF+1%CdS/ZnS and PVDF+10%CdS/ZnS is 10-40 nm, and 40-80 nm, respectively. XRD and SEM analysis of nanocomposites showed that CdS and ZnS nanoparticles don't form a solid solution in the PVDF matrix, but are distributed in the polymer as a separate dispersed phase [9,10.11].

Figures 3 and 4 show 3D AFM images and a histogram of the root-mean-square roughness of PVDF+CdS/ZnS based nanocomposites. It was found that with an increase in the content of CdS and ZnS nanoparticles, the supramolecular structure of polymer nanocomposites changes. Thus, the average roughness of a nanocomposite based on PVDF+1%CdS/ZnS is 10-70 nm, and for PVDF+10%CdS/ZnS is 20-140 nm. AFM analysis of nanocomposites shows that at low concentrations of nanoparticles, in contrast to high concentrations, a relatively smooth and ordered structure is formed.

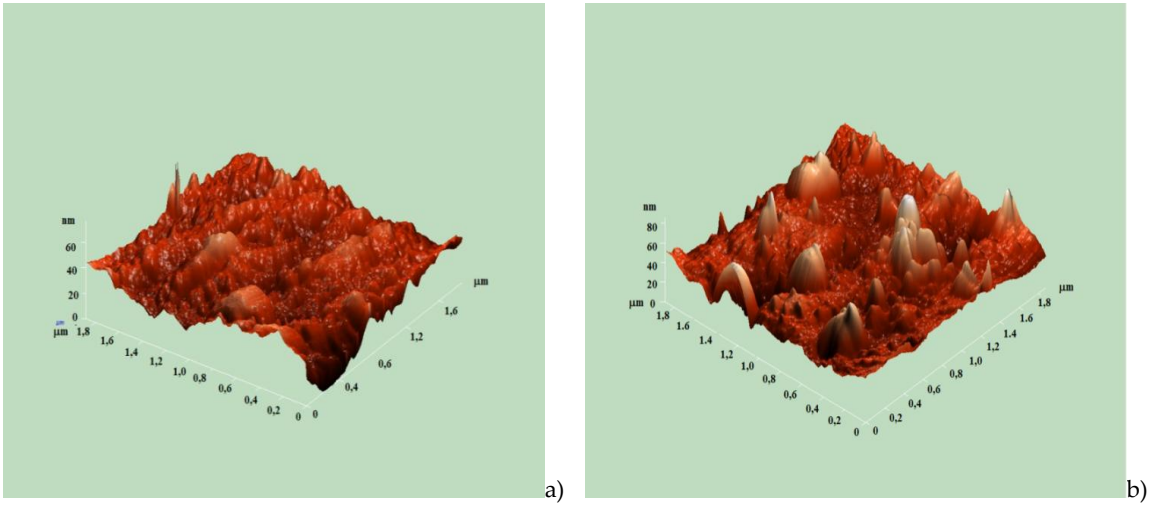

a) b)

Fig.3 AFM 3D images of PVDF+CdS/ZnS based nanocomposites: a) PVDF+1%CdS/ZnS; b) PVDF+10%CdS/ZnS.

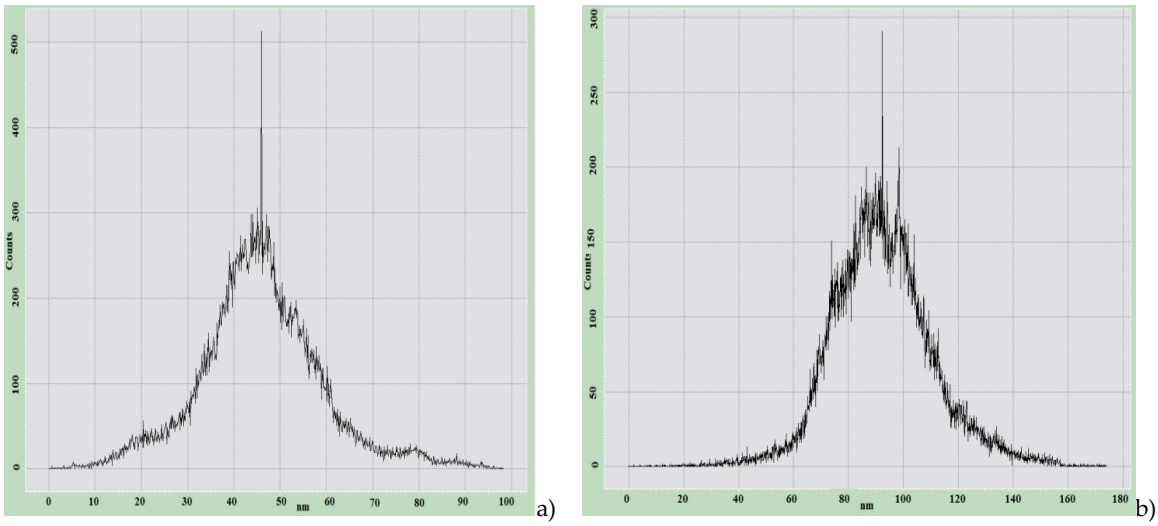

a) b)

Fig.4 Histogram of the root-mean-square roughness of PVDF+CdS/ZnS based nanocomposites: a) PVDF+1%CdS/ZnS; b) PVDF+10%CdS/ZnS.

Figure 5 (a) shows the optical absorption edge of PVDF+ZnS, PVDF+CdS and PVDF+CdS/ZnS based nanocomposites. From the literature data it is known that a decrease of the size of semiconductor nanoparticles leads to a shift in the edge of the UV spectrum to the blue part of the spectrum (T.Serrano, et.al, 2014) [12]. It was found that for nanocomposites based on PVDF+ZnS, the band gap is 3.6 eV, for PVDF+CdS, 3.0 eV, and PVDF+CdS/ZnS nanocomposite- 4.5 eV. We should note that for bulk cadmium sulfide with a wurtzite crystal structure, the band gap is 2.4 eV and for bulk zinc sulfide with a wurtzite crystal structure- 3.4 eV. Figure 5 (b) shows the optical absorption edge for nanocomposites based on PVDF+ CdS/ZnS depending on the concentration of ZnS and CdS nanoparticles. It was found that the band gap for hybrid nanocomposites based on PVDF+CdS/ZnS decreases with an increase in the content of ZnS and CdS nanoparticles. Thus, for a nanocomposite based on PVDF+1% CdS/ZnS, the band gap is 5.3 eV; for PVDF+3%CdS/ZnS- 5.0 eV, for PVDF+5%CdS/ZnS- 4.3 eV, for PVDF+10%CdS/ZnS- 3.1 eV. The decrease in the band gap can be explained with an increase in the particle size by an increase in the content of CdS and ZnS nanoparticles in the PVDF matrix. Chunchun and et.al in work [13] have developed epoxy-ZnO/CdS based hybrid nanocomposites and determined that these materials exhibit strong absorption in the wavelength range from UV to blue light in compare of ZnO nanoparticles, that absorb one part of the UV radiation.

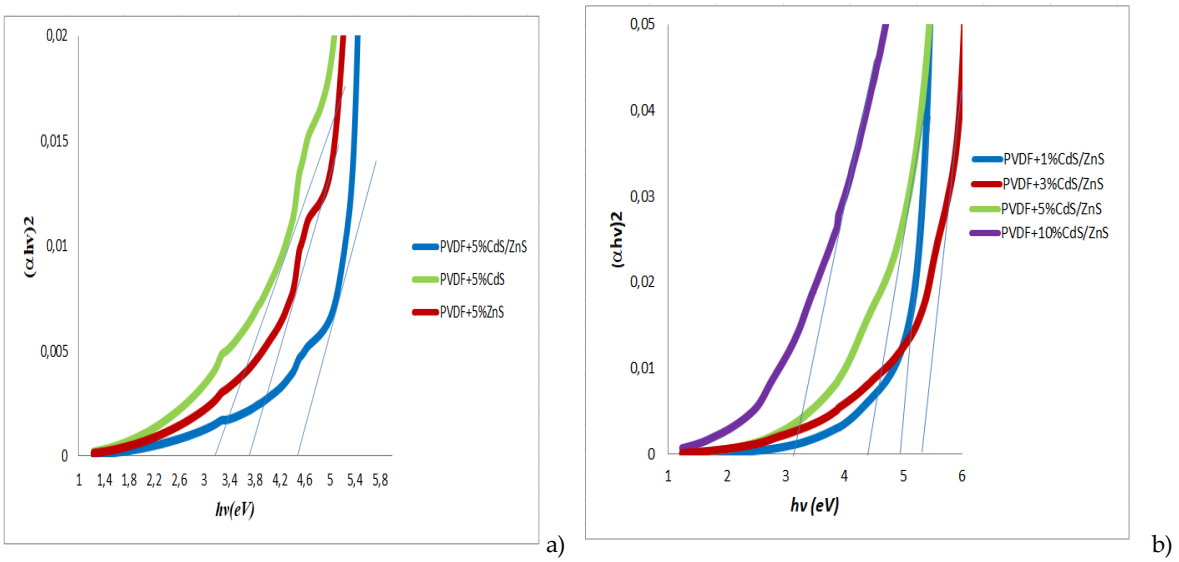

Fig.5 Optical absorption edge for nanocomposites based on PVDF+CdS, PVDF+ZnS and PVDF+CdS/ZnS.

Figure 6 shows the PL spectra of PVDF+CdS/ZnS nanocomposites depending on the content of CdS and ZnS nanoparticles. PL spectra were obtained upon excitation of nanocomposite films with light with a wavelength of λ=260 nm. It was found that the main peaks at 356 nm, 421 nm, 446 nm, 458 nm, 495 nm, 530 nm, 547 nm, 563 nm, 647 nm are luminescent peaks belonging to the hybrid PVDF+CdS/ZnS nanocomposite. As can be seen from the Figure 6, with an increase in the concentration of CdS and ZnS nanoparticles in the PVDF matrix to 3% of the content of nanoparticles, the PL intensity increases, and with a further increase in the content of nanoparticles, the PL intensity decreases. This is explained by the fact that with an increase in the concentration of CdS and ZnS nanoparticles, their size increases and the specific surface decreases, and this leads to a decrease in the contact area between the polymer and the nanoparticle.

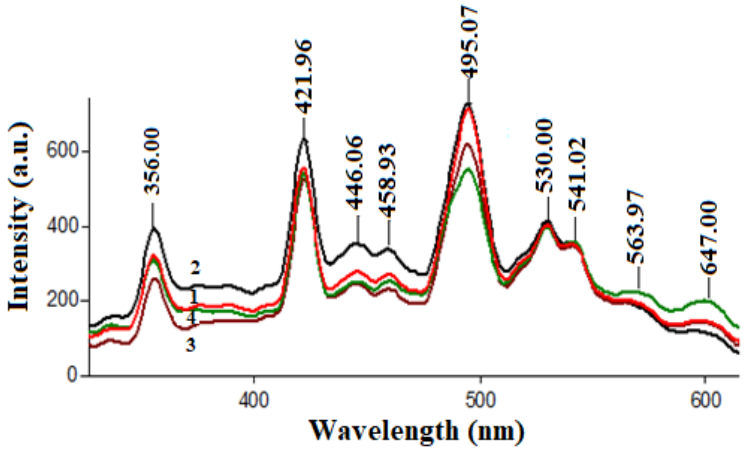

Fig. 6 PL spectra of polymer nanocomposites.

1. PVDF+1%CdS/ZnS; 2. PVDF+3%CdS/ZnS; 3.PVDF+5%CdS/ZnS; 4. PVDF+10%CdS/ZnS.

A decrease in the interfacial boundary leads to a decrease in interfacial interactions, and this, in turn, to a change in the PL intensity. It has been determined that the combined combination of photosemiconductor CdS and ZnS nanoparticles leads to a broadening of the spectral sensitivity. Photoluminescence analysis shows that for nanocomposites with a hybrid combination of quantum dots, luminescence is observed over a wide range of wavelengths [13-17]. Ramazanov and et.al in work [18] studied of hybrid polymer nanocomposites based on PP+PbS/CdS and observed that these nanocomposites exhibit intensive photoluminescence in the near infrared range at 680 nm and 715 nm [19-21].

Therefore, it has been established that hybrid nanocomposites can emit the light at a wide wavelength range, which makes it possible to use these nanocomposites in various fields: displays, converters, as active elements for solar cells applications, etc.

4. Conclusion

In the paper have been developed hybrid nanomaterials for solar cells applications. By UV spectroscopy, the optical absorption edges of the polymer nanocomposites have been determined and established that with an increase in the concentration of nanoparticles in the PVDF matrix, the band gap decreases. SEM and X-ray analysis showed that the nanoparticles are distributed in the polymer as a separate phase and do not form a solid solution in the polymer. Photoluminescence analysis shows that for nanocomposites with a hybrid combination of quantum dots, luminescence is observed over a wide range of wavelengths.

REFERENCE LIST

1. Ibáñez, M., Genç, A., Hasler, R., Liu, Y., Dobrozhan, O., Nazarenko, O., Mata, M., Arbiol, J., Cabot, A., & Kovalenko, M. (2019). Tuning transport properties in thermoelectric nanocomposites through inorganic ligands and heterostructured building blocks. *ASC Nano, 13*, 6572-6580.
2. Garjan, A., Farazin, J., Givi, G., & Azizian, Y. (2021). Formation of CdS/ZnS nanoparticles in polymer matrix by SILAR method: Experiments and exploring its optical properties with DDA calculations.*Optik. 242*,166958.
3. Petrella, A., Striccoli, M., Curri, M., &Agostiano, A. (2018). Optical properties of nanocomposites based on (CdSe)ZnS core shell nanocrystals in cyclic olefin copolymer. *Synth. Met. 245*,121-126.
4. Hadavand, M., Jafari, M., Pakpour, F., & Ghanbari, D. (2021). CdS/ZnS nanocomposite: synthesis and utilization in organic light-emitting diodes for a lower turn-on voltage. *J Nanopart Res*. *23*, 61.

5. Kundu, J., Satpathy, B., & Pradhan, D. (2019). Composition-controlled CdS/ZnS heterostructure nanocomposites for efficient visible light photocatalytic hydrogen generation. *Ind.Eng.Chem.Res. 58*, 22709-22717.
6. Yang, F., Zhang, Q., Huang, S., & Dongling, M. (2020). Recent advances of near infrared inorganic fluorescent probes for biomedical applications. *J. Mater. Chem. B*. *8*,7856-7879.
7. Yingming,S., Pan,H., Chu,H., Mamat, M., Abudurexiti, A., & Li, D. (2021) Core-shell CdSe/ZnS quantum dots polymer composite as the saturable absorber at 1.3 μm: Influence of the doping concentration. *Phys. Lett. A*. *400*,127307.
8. Hao, J., Liu, H., Miao, J., Lu, R., Zhou, Z., Zhao, B., Xie, B., Cheng, J., Wang, K., & Delville, M. (2019). A facile route to synthesize CdSe/ZnS thick-shell quantum dots with precisely controlled green emission properties: towards QDs based LED applications. *Sci.Rep. 9 (1),*12048.
9. Yoon, C., Yang, K., Kim, J., Shin, K., & Lee, K. (2020). Fabrication of highly transparent and luminescent quantum dot/polymer nanocomposite for light emitting diode using amphiphilic polymer-modified quantum dots *Chem. Eng. J. 382*, 122792.
10. Han, C., Wang, F., Gao, C., Liu, P., Ding,Y., Zhanga, S., & Yang, M. (2015). Transparent epoxy–ZnO/CdS nanocomposites with tunable UV and blue light-shielding capabilities. *J. Mater. Chem. C.3,19*, 5065–5072.
11. Lee, D., Kim, D., Choi, D., Kim, S., Lee, H., Yoo, K., & Kim, T. (2016). Microstructural and optical properties of CdSe/CdS/ZnS core-shell-shell quantum dots *Opt. Express*. *24 (2),* A350-A357.
12. Boercker, J., Woodall, D., Cunningham, P., Placencia, D., Ellis, C., Stewart, M., Brintlinger, T., Stroud, R., & Tischler, J. (2014). Synthesis and characterization of PbS/ZnScore/shell nanoparticles by microwave method, *Chalcogenide Lett. 11 (1),* 21-28.
13. Han, C., Wang, F., Gao, C., Liu, P., Ding, Y., Zhanga Sh., & Yang, M. (2015). Transparent epoxy- ZnO/CdS nanocomposites with tunable UV and blue light-shielding capabilities, *J. Mater. Chem. C. 3*, 5065–5072.
14. Chen, Y., Wei, L., Zhang, G., & Jiao, J. Open structure ZnO/CdSe core/shell nanoneedle arrays for solar cells. *Nanoscale Res. Lett.*, *7(1),* 516.
15. Gordillo, H., Suárez, I., Abargues, R., Cantó, P., Albert, S., & Martínez-Pastor, J. (2012) Polymer/QDs Nanocomposites for Waveguiding Applications. *J. Nanomater. 2012,* 33.
16. Wildner, W., & Drummer, D. (2018). Nanofiller materials for transparent polymer composites: Influences on the properties and on the transparency- A review *J. Thermoplast. Compos. Mater. 32(11),* 1547–1565.
17. Ramazanov, M., Hajiyeva, F., Babayev, Y., Valadova, G., Nuriyeva, S., & Shirinova, H. (2019). Synthesis and optical properties of PVC-CdS-based nanocomposites *J. Elastomers Plast. 52(2),*159-166.
18. Ramazanov, M., Chianese, A., Hajiyeva, F., & Novruzova, A. (2019). Structure and photoluminescence properties of hybrid nanocomposites on the base of PP/PbS/CdS *Integr. Ferroelectr. 201 (21),* 55-61.
19. Ramazanov, M., & Hajiyeva, F. (2019). Influence of crystallization temperature–time technological factors on structure and photoluminescence properties of polymer nanocomposites on the base of isotactic polypropylene (PP) and lead sulphide (PbS) nanoparticles, *J. Inorg. Organomet. Polym. Mater. 29 (6),* 2168–2175.
20. Nuriyeva, S., Shirinova, H., Hasanov, K., & Hajiyeva, F. (2023). Controlled synthesis of silver nanowires: production and characterization *Acta Physica Polonica A 143(4),* 277-344.
21. Ramazanov, M., Hajiyeva, F., Maharramov, A., Ahmadova, A., Hasanova, U,., Rahimli, A., & Shirinova, H. (2017). A influence of polarization process on morphology and photoluminescence properties of PP/TiO_2 nanocomposites *Acta PhysicaPolonica A*, *131,* 1540-1543.

JOURNAL OF BAKU ENGINEERING UNIVERSITY - PHYSICS
2025. Volume 9, Number 1 *Pages 29-34*

UDC:539.23:535.34
DOI: https://doi.org/10.30546/09081.2025.001.8024

THE EFFECT OF NANOQUARTZ ON THE OPTICAL PROPERTIES OF IPP

H.S. İBRAHIMOVA

Institute of Physics, Ministry of Science and Education of Azerbaijan,
Baku, Azerbaijan

ARTICLE INFO

Article history
Received:2025-04-08
Received in revised form:2025-06-19
Accepted:2025-10-14
Available online

Keywords:
nanoquartz;
isotactic polypropylene;
transmission spectra;
absorption spectra;
Urbach energy

ABSTRACT

This study investigates the effect of nanoquartz (SiO_2) nanoparticles on the optical properties of isotactic polypropylene (iPP) composites. SiO_2 was added to iPP at various concentrations (1%, 3%, 5%, 7%, and 10%) to investigate changes in optical transmission, absorption spectra, and optical band gap. The results show a decrease in optical transmission as the SiO_2 concentration increases, with the material exhibiting stronger scattering and absorption effects. The absorption edge shifts toward longer wavelengths (redshift), indicating a narrowing of the optical band gap. This change was further confirmed by the Tauc method, which showed a decrease in band gap with increasing nanoparticle content. In addition, the Urbach energy, which reflects material disorder, was observed to increase with higher SiO_2 concentrations. This suggests that the incorporation of nanoparticles introduces localized defects and structural inhomogeneities into the polymer matrix. These results demonstrate that nanoquartz SiO_2 significantly modifies the optical behavior of iPP composites, enhancing their potential for use in optoelectronic devices where controlled optical properties such as light absorption and bandgap tuning are critical to performance.

1. Introduction

Polymers and polymer nanocomposites are widely used in all fields of science and technology. The use of solid nanoparticles as fillers opens up new possibilities for their application. With the addition of metal oxide nanoparticles in nanotechnology, new opportunities for their use arise [1,2,3]. Most of the scientific research in the field of polymer nanocomposites is dedicated to the application of metal oxides as fillers. Polymer-metal oxide nanocomposites, as composite materials, possess a number of unique properties [4,5,6]. Qualitatively new effects, properties and processes determined by quantum mechanics appear, improving certain properties: their electrophysical, strength, thermal stability and resistance to aggressive environments. They can be used as materials for photocatalysts, bioimaging, and also as sensors in optoelectronic materials. Polymer-metal oxide nanocomposites hold great promise in the fields of optics and optoelectronics, offering unique opportunities for the development of new devices and technologies [7,8]. Various studies have investigated the optical properties of polymer-metal oxide nanocomposites. However, the optical properties as a function of the percentage of nanofiller content, the changes in the optical properties depending on the size of the nanofiller, as well as the changes due to external influences for nanocomposites made of isotactic PP and nanocrystalline SiO2 are still insufficiently studied. These factors are among the most important

issues in the selection of materials for research. Among polymeric materials, polypropylene (PP) is one of the polymers that has attracted significant interest due to its transparent and colorless properties. It has a long service life and excellent mechanical and chemical stability. The aim of this work is to investigate the optical properties of polymer nanocomposites. The choice of nanocrystalline silica as nanofiller for polymer nanocomposites is justified by their unique optical and mechanical properties, which allow the creation of materials with improved properties for various optical applications.

2. Experiments

For the composite matrix, isotactic PP granules with a size of 5 mm (Dema Import and Export Co. Ltd., China) with a density of 0.92 g/cm^3, a molecular weight of 300-700 thousand and a specific volume resistivity of 10^{14}-10^{15} Ω-m were used. The filler used in the study was nanocrystalline SiO_2 with particle sizes ranging from 25 to 35 nm and a density of 2.6 g/cm3 (Sigma-Aldrich, St. Louis, Missouri, USA). The preparation of PP+SiO_2 nanocomposites was carried out by introducing nanoparticles into a polymer solution [9]. The composites were obtained by hot pressing at the melting temperature of the polymer matrix under a pressure of 15 MPa for 10 min. Films with a thickness of 85 μm were prepared. The forbidden band energy was evaluated experimentally by measuring the variation of optical absorption intensity as a function of photon energy over a wide range from visible to vacuum ultraviolet wavelengths. Optical spectra in the UV and visible regions were measured using a Specord-250 spectrophotometer. The absorption spectra of the polymer-metal oxide nanoparticles were analyzed using the Tauc method to determine the band gap by approximating the curves [10]. By reconstructing the absorption spectrum and extrapolating the linear region of the spectrum to the abscissa axis, the width of the forbidden zone was obtained. The direct allowed band gap energy was calculated from the curves.

3. Results and discussion

Figure 1 shows the optical transmission spectra of the PP+SiO_2 nanocomposites at different filler volume fractions. At low filler content, the transmission coefficient decreases as the percentage of nanofiller increases. The transmission of the thin PP film is about 89%. The transmission edge for the polymer doped with metal oxide nanoparticles shifts to lower energies (red shift) compared to pure PP at room temperature. The strong interaction between the metal oxide nanoparticles and the polymer matrix leads to a change in crystallinity, which in turn changes the band structure and absorption percentage.

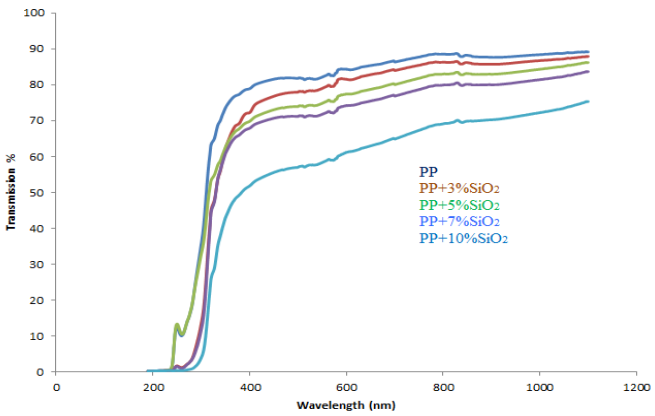

Fig. 1 Optical transmission spectra of PP+SiO_2 nanocomposites at different filler volume fractions.

These changes are associated with physicochemical processes occurring at the nanoscale, which depend on the type of nanoparticles, their concentration, and the nature of the polymer matrix. The addition of nanoparticles can cause changes in the microstructure of the polymer composite, which in turn affects the optical properties of the material. Nanoparticles can also interact with the polymer matrix, altering its energy state. This interaction may reduce the energy band gap, leading to a shift in the transmission edge towards longer wavelengths. As the percentage of SiO_2 increases, these nanoparticles may experience stronger inter-particle interactions, which could result in agglomeration, increased light scattering, and reduced transmission. Absorption increases with the nanoparticle content, as the free electrons in the nanoparticles can absorb the incoming radiation.

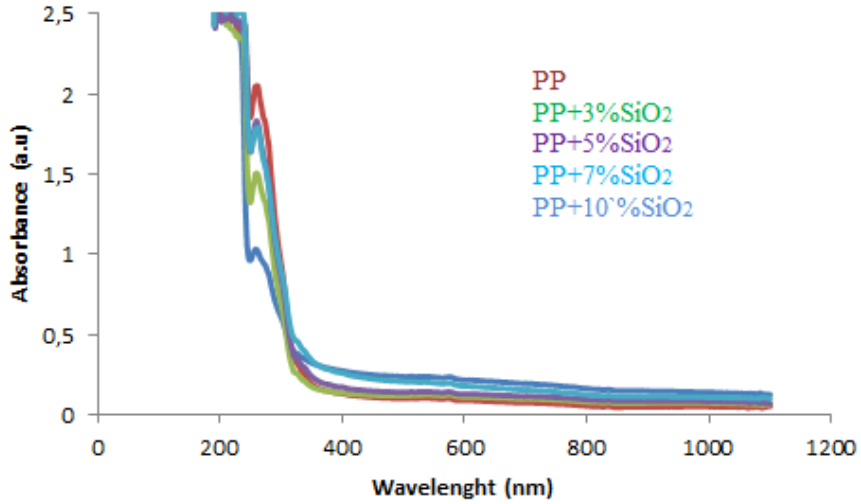

Fig. 2 Absorption spectra for the PP+SiO_2 nanocomposites.

From figure 2, a peak in the short wavelength region can be observed, which can be related to the presence of unsaturated (ethylene and carbonyl) groups in the structure of the blend [11]. This peak shifts towards longer wavelengths as the nanoparticle content increases, indicating a reduction in the band gap, an increase in the amorphous structure of the films and an improvement in the semiconducting behavior of the resulting films.

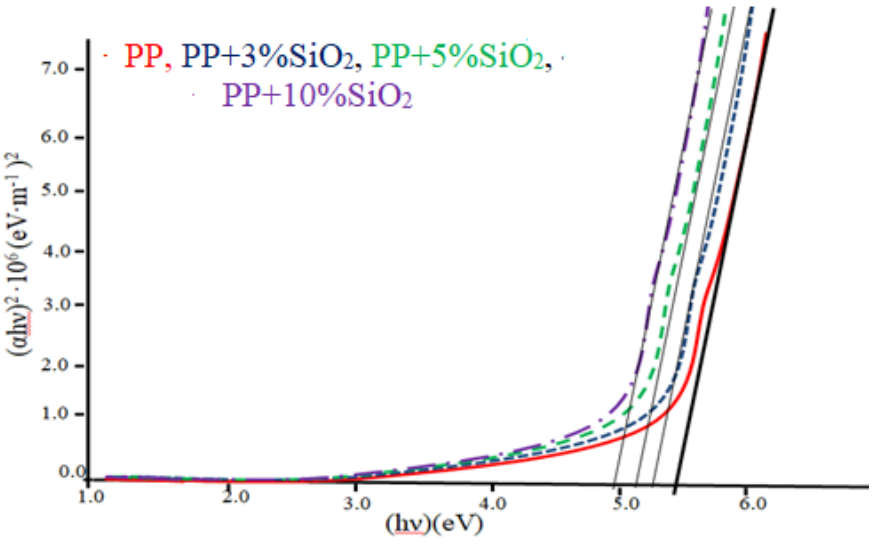

Fig. 3 Width of band gap of nanocomposites.

According to the Tauc theory

$$\alpha h\nu = B(h\nu - E_g)^P \quad (1)$$

where: α-alpha is the absorption coefficient, hν is the photon energy, Eg is the optical band gap, B is a constant that depends on the material and the type of optical transition (direct or indirect), the index P refers to the distribution of the density of states. This index can take values of 1/2,3/2, 2, or 3 depending on the nature of the electronic transition. In this case, P=2

Figure 3 shows the dependence of the absorption coefficient on the photon energy for the nanocomposites. As shown in the figure, the band gap of the pure polymer is larger than that of the nanocomposites for all types of nanofillers. Doping with metal oxide nanoparticles affects the transmission band of the polymer structure. As the nanofiller concentration increases, the optical band gap decreases. Thus, effective control of the transmission band can be achieved by introducing a specific concentration of nanofillers into the polymer matrix.This effect can be explained by the interaction between the nanoparticles and the polymer matrix, which changes the local distribution of electronic states. Such interactions can modify the energy of electronic transitions within the composite, thereby influencing the bandgap width. In addition, as the concentration of nanoparticles in the polymer matrix increases, the electronic structure of the material changes due to changes in interparticle interactions and the state of surface atoms. The addition of nanoparticles alters the density of states at the polymer-nanoparticle interface, leading to changes in the electronic structure and consequently the bandgap [12]. The introduction of nanofillers can modify the dynamics of electronic transitions in the material by interacting with phonons (lattice vibrations). Depending on the nature of these interactions, the band gap width can either increase or decrease.

Thus, the variation in bandgap width with increasing nanofiller concentration in polymer composites is attributed to the quantum size effect, interphase interactions, and changes in the electronic structure of the material. According to Urbach's theory [13], an increase in disorder within a material leads to a broadening of the band edges and a reduction in the band gap width. When nanoparticles are introduced into the polymer matrix, they can create local perturbations in the polymer structure. These perturbations can include structural defects, inhomogeneities, and interfacial interactions between the polymer and the filler. Such perturbations increase the disorder in the system, which, according to Urbach's theory, can result in a reduction of the band gap width and a shift of the absorption edge toward the long wavelength region of the spectrum. Therefore, as the percentage of nanofillers in the polymer matrix increases, the structural disorder intensifies, leading to a decrease in the band gap width and the appearance of a more pronounced "Urbach tail". This also leads to changes in the optical properties of the nanocomposites, which can be observed in the absorption and transmission spectra. The energy associated with this tail is known as the Urbach energy (Eν), which can be determined using the following relationship [14]:

$$\alpha(\nu) = \alpha_0(\nu)exp\frac{h\nu}{E_\nu} \quad (2)$$

The Urbach energy in polymer composites characterizes the distribution of energy levels within the band gap and indicates how rapidly light absorption decreases as photon energy increases. [15,16]

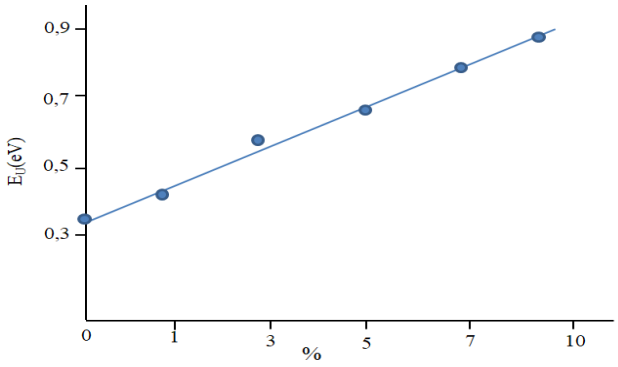

Fig. 4 Dependence of Urbach energy on the nanofiller concentration for the PP+SiO_2 composite

Figure 4 shows the dependence of the Urbach energy on the concentration of composites. As can be seen, the Urbach energy increases with increasing nanofiller concentration.This increase is likely due to the creation of additional surface defects and disordered regions within the polymer that affect the energy levels and density of states at the valence and conduction band edges. This structural disorder contributes to the increase in the Urbach energy, which characterizes the degree of disorder in the material.

4. Conclusion

The incorporation of nanoquartz SiO_2 into isotactic polypropylene significantly alters its optical properties by reducing transmittance, shifting the absorption edge, narrowing the band gap, and increasing the Urbach energy. These changes are attributed to nanoparticle-induced changes in electronic structure, interfacial interactions, and quantum confinement effects. The results highlight the potential of iPP + SiO_2 nanocomposites in optical and optoelectronic applications where controlled light absorption and tailored bandgap properties are required.

REFERENCE LIST

The Journal follows APA Style Referencing:

Book chapters: Author, A. A., Author, B. B., & Author, C. C. (Year). Title of the chapter. In the *title of the book* (pages). Publisher.

- Tamayo, L., Palza, H., & Bejarano, J. (2019). Polymer composites with functionalized nanoparticles. In Zapata, P. A. (Ed.), Polymer-based nanocomposites for energy and environmental applications (pp. 249–286). Elsevier. https://doi.org/10.1016/B978-0-12-814064-2.00008-1.
- Tauc, J. (1974). Optical properties of amorphous semiconductors. In Tauc, J. (Ed.), Amorphous and Liquid Semiconductors (pp. 159–200). Plenum Publishing Co. https://doi.org/10.1007/978-1-4615-8705-7

JOURNAL ARTICLES:

12. Bhol, P., Mohanty, M., & Mohanty, P. S. (2021). Polymer-matrix stabilized metal nanoparticles: Synthesis, characterizations and insight into molecular interactions between metal ions, atoms and polymer moieties. Journal of Molecular Liquids, 325, 115135. https://doi.org/10.1016/j.molliq.2020.115135
13. Dikshit, P. K., Kumar, J., & Das, A. K. (2021). Green synthesis of metallic nanoparticles: Applications and limitations. Catalysts, 11(8), 902. https://doi.org/10.3390/catal11080902
14. Ghazzy, A., Naik, R. R., & Shakya, A. K. (2023). Metal–polymer nanocomposites: A promising approach to antibacterial materials. Polymers, 15(9), 2167. https://doi.org/10.3390/polym15092167
15. Zadehnazari, A. (2022). Metal oxide/polymer nanocomposites: A review on recent advances in fabrication and applications. Polymer-Plastics Technology and Materials, 62(5), 655–700. https://doi.org/10.1080/25740881.2022.2129387

16. Hilmi, A. R., & Purnamasari, N. D. (2022). Thermomechanical and optical characteristics of nanoquartz- and nanozircon-filled poly(methyl methacrylate) composites. Journal of Applied Polymer Science, 139, 52923. https://doi.org/10.1002/app.52923
17. Nguyen, T. P. (2011). Polymer-based nanocomposites for organic optoelectronic devices: A review. Surface and Coatings Technology, 206(4), 742–752. https://doi.org/10.1016/j.surfcoat.2011.07.010
18. Nakata, K., & Fujishima, A. (2012). TiO_2 photocatalysis: Design and applications. Journal of Photochemistry and Photobiology C: Photochemistry Reviews, 13, 169–189. https://doi.org/10.1016/j.jphotochemrev.2012.06.001
19. Ibrahimova, H. S., Rzayev, R. M., & Mustafayeva, E. M. (2024). Thermophysical properties of PP/ZrO_2 nanocomposites before and after electrothermal polarization. Journal of Inorganic and Organometallic Polymers and Materials, 4655–4660. https://doi.org/10.1007/s10904-024-03062-y
20. Al-Muntaser, A. A., Abdelghany, A. M., & Abdelrazek, E. M. (2020). Enhancement of optical and electrical properties of PVC/PMMA blend films doped with $Li_4Ti_5O_{12}$ nanoparticles. Journal of Materials Research and Technology, 9(1), 789–797. https://doi.org/10.1016/j.jmrt.2019.11.019
21. Sharifov, D., Niyazbekova, R., Mirzo, A., Shansharova, L., Serekpayeva, M., Aldabergenova, S., Ibzhanova, A., Machnik, R., & Bembenek, M. (2024). The study of composite materials properties based on polymers and nano-additives from industrial wastes from Kazakhstan. Materials, 17(12), 2959. https://doi.org/10.3390/ma17122959
22. Studenyak, I., Kranjec, M., & Kurik, M. (2014). Urbach rule in solid state physics. International Journal of Optics and Applications, 4(3), 76–83. https://doi.org/10.5923/j.optics.20140403.02
23. Urbach, F. (1953). The long-wavelength edge of photographic sensitivity and of the electronic absorption of solids. Physical Review, 92, 1324. https://doi.org/10.1103/PhysRev.92.1324
24. Ota, M., Ando, S., Endo, H., Ogura, Y., Miyazaki, M., & Hosoya, Y. (2011). Influence of refractive index on optical parameters of experimental resin composites. Acta Odontologica Scandinavica, 70(5), 362–367. https://doi.org/10.3109/00016357.2011.600724
25. Darwesh, A. H. A., Aziz, S. B., & Hussen, S. A. (2022). Insights into optical band gap identification in polymer composite films based on PVA with enhanced optical properties: Structural and optical characteristics. Optical Materials, 113007. https://doi.org/10.1016/j.optmat.2022.113007

JOURNAL OF BAKU ENGINEERING UNIVERSITY - PHYSICS
2025. Volume 9, Number 1 *Pages 35-42*

UDC 535.34:537.311.33
DOI: https://doi.org/10.30546/09081.2025.001.8005

ABSORPTION AND BAND STRUCTURE MODIFICATION IN BORON-SUBSTITUTED GaSe

Lamiya BALAYEVA[1*], Ali GUSEINOV[2]

[1]*Department of Semiconductor physics,*
Baku State University,
Baku, Azerbaijan
[2]*Department of Semiconductor physics,*
Baku State University,
Baku, Azerbaijan

ARTICLE INFO

Article history
Received:2025-09-29
Received in revised form:2025-11-06
Accepted:2025-11-18
Available online

Keywords:
Optical properties,
Layered chalcogenide semiconductors,
Band gap narrowing,
Electronic band structure modification,
Visible and near – infrared photodetection

ABSTRACT

Single crystals $Ga_{1-x}B_xSe$ *(x = 0.3 and 0.5%) were synthesized using the horizontal Bridgman method, and their optical characteristics were systematically examined. UV–Vis absorption spectra revealed a direct band gap of 1.960–1.963 eV, slightly narrower than that of undoped GaSe (≈ 2.0 eV). This reduction originates from lattice distortions and electronic perturbations introduced by boron atoms, which shift the absorption edge toward longer wavelengths, improving the material's suitability for visible and near-infrared photodetection. Additional absorption features at 1.05 eV and 1.35 eV correspond to boron-induced impurity states that affect the temperature dependence of absorption. At lower boron concentrations, the absorption coefficient increases with temperature due to thermal excitation, while at higher concentrations, a negative temperature coefficient appears, indicating enhanced radiative recombination. These results demonstrate that controlled boron incorporation effectively tailors the band structure and optical response of GaSe, enabling its application in broadband optoelectronic and photodetector devices.*

[*] Corresponding author.*E-mail addresses*: *blamiye99@gmail.com (Lamiya Balayeva).*

1. Introduction

Gallium selenide (GaSe) is a III–VI semiconductor with a layered structure that crystallizes in four distinct polymorphic forms: β, γ, δ, and ε [1]. Among these, ε–GaSe is of particular significance due to its diverse optical applications. Devices based on ε–GaSe include photodetectors [2–4], phototransistors [5,6], energy storage systems [7], and nonlinear optical applications [8–10]. Furthermore, the bandgap of ε–GaSe can be tuned either by applying external strain or by reducing its thickness to a few layers [11–16], thereby opening up new opportunities for the development of next-generation devices [11,17]. The epitaxial properties of ε–GaSe also enable compatibility with other two-dimensional (2D) materials, facilitating the fabrication of ultrathin heterojunctions and their subsequent application in various optoelectronic devices [8,18]. More broadly, chalcogenides such as GaSe are highly attractive for non-resonant applications owing to their strong nonlinear optical response and large real refractive index [19]. In addition, the high absorption coefficient of GaSe makes it suitable as a

light-absorbing material in solar cells. Thus, the study of its optical parameters is of particular importance, as it provides a deeper understanding of the material's optical quality.

In general, to achieve a comprehensive understanding of the optical and electronic behavior of any material, parameters such as the refractive index (n), extinction coefficient (k), absorption coefficient (α), and band structure characteristics are essential. Specifically, accurate determination of the wavelength dependence of the complex refractive index N(λ) and the complex dielectric function $\varepsilon(\lambda)$ yields critical insights into the dispersion and absorption features of the material, which are crucial for its implementation in optoelectronic devices [20,21]. It should be noted that these fundamental optical parameters are related not only to $\alpha(\lambda)$ but also to the reflectance R(λ). However, precise determination of R(λ) remains an open issue that requires particular attention. Moreover, in many cases, the computational methods employed provide reliable results only within the transparency region [22–26]; outside this range, inaccuracies may arise, potentially leading to misinterpretation of experimental results.

Considering these aspects, the determination of the optical parameters of $Ga_{1-x}B_xSe$ (x = 0.3, 0.5%) crystals synthesized by us is of great significance, both for obtaining comprehensive information about these crystals and for identifying their potential application areas. For this reason, in the present work, a solid solution $Ga_{1-x}B_xSe$ was synthesized by substituting part of the gallium (Ga) atoms with boron (B) atoms. The grown single crystals were then investigated in detail to determine their optical parameters.

2. Experimental details

2.1. Growing of $Ga_{1-x}B_xSe$ crystals

The $Ga_{1-x}B_xSe$ solid solution was synthesized in evacuated quartz ampoules through direct melting of the constituent elements, with a total mass of 15 g. The reaction proceeded via an exothermic pathway. To mitigate excessive pressure accumulation within the ampoule, one end of the sealed tube was externally cooled, while the opposite end was gradually heated in an electric furnace to 1100 °C. Upon completion of the initial reaction, the ampoule was transferred to an isothermal furnace maintained at 1100 °C and subjected to an annealing process lasting 4 h, thereby ensuring compositional homogenization. The resulting ingot displayed uniform chemical composition and was characterized by the presence of large crystalline domains. This ingot was subsequently ground into a fine powder and reloaded into a quartz ampoule. After evacuation to a residual pressure of 10^{-5} Pa, the ampoule was hermetically sealed and utilized for single-crystal growth employing the horizontal Bridgman technique. Macroscopic examination of the as-grown crystals revealed a dark-red coloration accompanied by a distinct layered morphology, features that are typical of GaSe-based compounds.

2.2. Characterization techniques

The photoelectric characteristics of the samples were examined under high-vacuum conditions using a closed-cycle cryostat system. This setup enabled comprehensive measurements across a broad temperature range from 110 K to 400 K and within the optical spectral range of 480–2000 nm, facilitating the investigation of temperature-dependent carrier transport and spectral response behavior.

The optical characteristics of the samples were further examined using a Specord 250 Plus UV–Vis spectrophotometer across the spectral range of 190–1100 nm, providing comprehensive insight into their absorption behavior.

3. Result and discussions

Figure 1(a) presents the absorption spectrum of the $Ga_{0.997}B_{0.003}Se$ crystal at room temperature. As can be seen, a pronounced absorption edge appears around 650 nm. Beyond this threshold, the absorption intensity decreases sharply with increasing wavelength and becomes nearly constant above approximately 700 nm. Such behavior is characteristic of a material possessing a direct band gap. Figure 1(b) illustrates the dependence of $(\alpha h\nu)^2$ on $h\nu$, from which the band gap was determined using the Tauc method. Analysis yielded a band gap energy of approximately 1.963 eV, which is slightly lower than the well-established value for pure GaSe (≈ 2.0 eV [27]). This reduction is attributed to the partial substitution of Ga atoms by B atoms. The smaller atomic radius of boron introduces local lattice distortions, leading to subtle modifications in the electronic energy levels and, consequently, a narrowing of the band gap. The band gap narrowing effectively extends the optical absorption range of GaSe towards longer wavelengths. This property is particularly advantageous for photodetector applications operating in the visible and near-infrared (NIR) spectral regions. Importantly, the sharpness of the absorption edge is preserved upon boron incorporation, indicating the high crystalline quality of the material. Thus, the controlled introduction of boron offers a viable means of tuning the spectral sensitivity of GaSe-based optoelectronic devices.

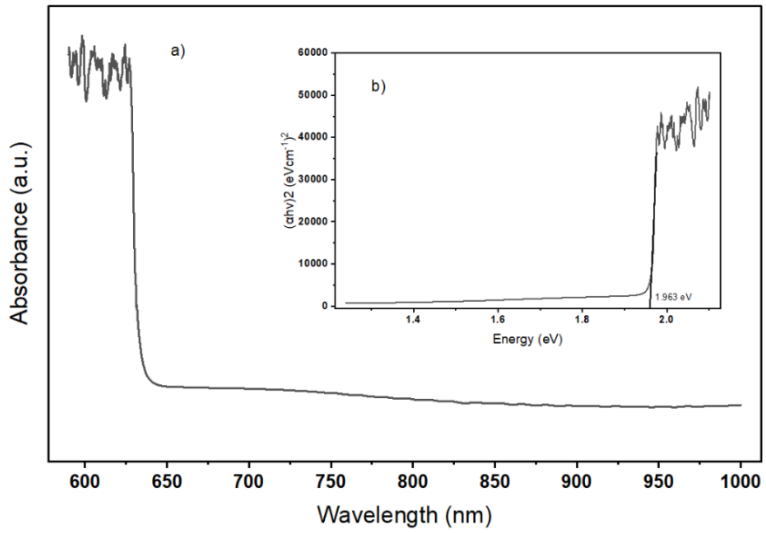

Fig. 1. (a) Absorption spectrum of the $Ga_{0.997}B_{0.003}Se$ crystal and (b) determination of the band gap energy based on the Tauc dependence.

Figure 2 presents the absorption spectra of a 120 μm thick $Ga_{0.997}B_{0.003}Se$ thin film measured at 300 K and 110 K. The spectra correspond to the long-wavelength edge of the intrinsic absorption band. Two distinct spectral features are observed at photon energies of approximately 1.05 eV and 1.35 eV. As reported in [28], the incorporation of boron atoms into GaSe crystals introduces impurity levels located at a depth of 1.05 eV. Given the layered structure of GaSe, it is most plausible that the boron atoms occupy interlayer positions. Nevertheless, under partial substitution of Ga atoms in the stoichiometric lattice of gallium selenide, boron atoms may also reside at vacant gallium sites, thereby engaging in chemical bonding with both selenium and gallium atoms. The optical transitions detected at an energy of 1.05 eV can reasonably be attributed to electron transitions from the $4P_1$ level of Ga (5.999 eV) to the $3S_2S_1/_2$ level of B (4.9663 eV). This interpretation supports the role of boron incorporation in modifying the electronic structure of GaSe and establishing localized impurity states within the band gap.

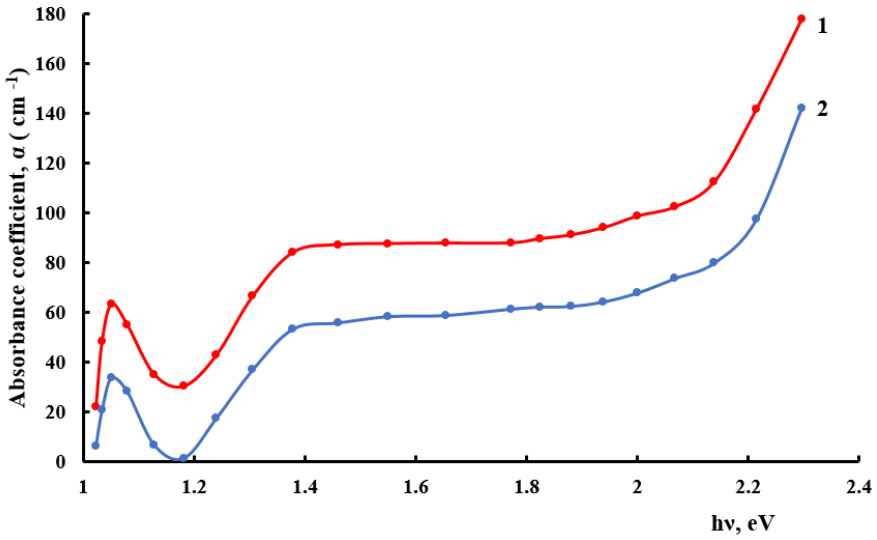

Fig. 2. Absorption spectra of the $Ga_{0.997}B_{0.003}Se$ crystal at 300 K (1) and 110 K (2)

The $Ga_{0.997}B_{0.003}Se$ crystals exhibit p-type conductivity, similar to that of pure GaSe. The optical absorption feature observed at 1.35 eV is most likely associated with electronic transitions from the acceptor level to the conduction band. The impurity-band absorption spectrum for a parabolic dispersion is described by the following expression [29]:

$$\alpha(h\vartheta) = \frac{32\pi e^2\hbar^2}{n_0 m_0}\,\frac{\varepsilon_{eff}}{\varepsilon}\,\left|\vec{e}\vec{P}_{cv}\right|\frac{m_e^*}{m_r R^*}\cdot\frac{S\,(\nu,x)}{h\nu}\,N_i F_{AB}$$

where n0 is the refractive index; $\frac{\varepsilon_{eff}}{\varepsilon}$ is the correction for the effective field, taking into account the dependence of the field in the crystal on its polarization; me* is the effective mass in the conduction band; mr is the reduced mass of an electron and a hole; R* is the effective Rydberg constant; (S (ν,x))/hν is the flux of photons with energy hν; Ni is the impurity concentration; FAB is the probability that the initial state is occupied and the final state is free. As the equation indicates, the absorption coefficient is strongly dependent on the concentration of electrons localized at the acceptor level. With increasing temperature, the population of these states rises due to thermal excitation of valence-band electrons into acceptor states, which in turn enhances the absorption coefficient. This temperature dependence is evident in Figure 1, where the absorption coefficient of $Ga_{0.997}B_{0.003}Se$ increases with rising temperature, indicating a positive temperature coefficient of absorption.

Figure 3(a) shows the absorption spectrum of the $Ga_{0.995}B_{0.005}Se$ crystal at T = 300 K. The absorption edge is clearly observed in the 635–650 nm interval. As the wavelength increases, the absorption decreases and becomes nearly constant beyond 700 nm. Figure 3(b) presents the Tauc plot, $(\alpha h\nu)^2$ on hν. From this analysis, the band gap energy was estimated to be approximately 1.960 eV. This value is very close to that obtained for the $Ga_{0.993}B_{0.003}Se$ crystal (≈ 1.963 eV) and slightly smaller than that of pure GaSe (≈ 2.0 eV). The results indicate that increasing the boron concentration does not lead to abrupt changes in the band gap but instead produces a gradual narrowing. This effect can be explained by local lattice distortions and modifications of electronic energy levels arising from the substitution of Ga atoms with smaller-radius B atoms. The

observed narrowing of the band gap suggests that the incorporation of boron allows for the spectral range of GaSe-based optoelectronic devices to extend towards the near-infrared region, thereby improving their applicability in broadband photodetection.

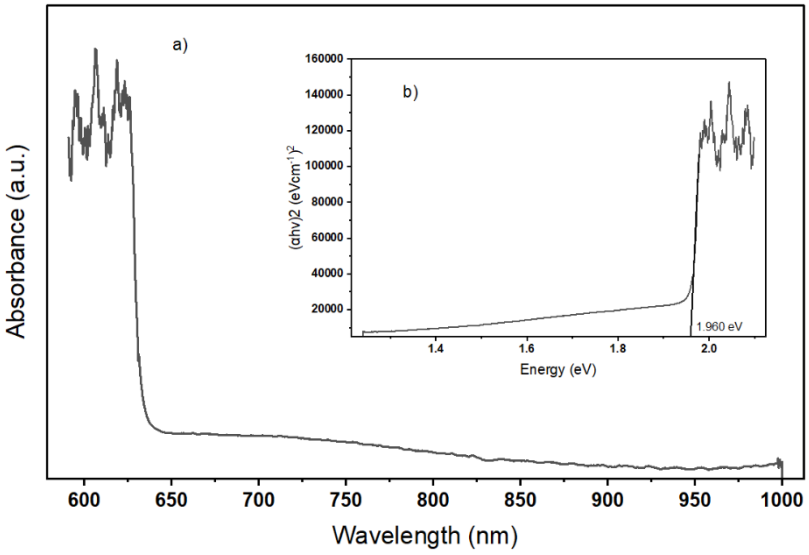

Fig. 3. (a) Absorption spectrum of the $Ga_{0.995}B_{0.005}Se$ crystal and (b) determination of the band gap energy based on the Tauc dependence.

The absorption coefficient spectrum of the $Ga_{0.995}B_{0.005}Se$ crystal at the long-wavelength edge of the fundamental absorption band exhibits a similar overall character to that of the previously studied spectrum (Fig. 4). However, in the $Ga_{0.995}B_{0.005}Se$ crystal, the absorption coefficient in the region around 1.05 eV is noticeably lower compared to the corresponding value in $Ga_{0.997}B_{0.003}Se$. Furthermore, in contrast to the earlier case, the temperature absorption coefficient of the $Ga_{0.995}B_{0.005}Se$ crystal assumes a negative sign. When the temperature is increased from 110 K to 300 K, the photoluminescence (PL) intensity of the crystals shows a slight enhancement. This observation suggests that the negative temperature dependence of the absorption coefficient is likely associated with an increase in radiative recombination of nonequilibrium charge carriers at elevated temperatures. Such behavior indicates a competition between optical absorption and recombination processes, with the latter becoming more significant as temperature rises.

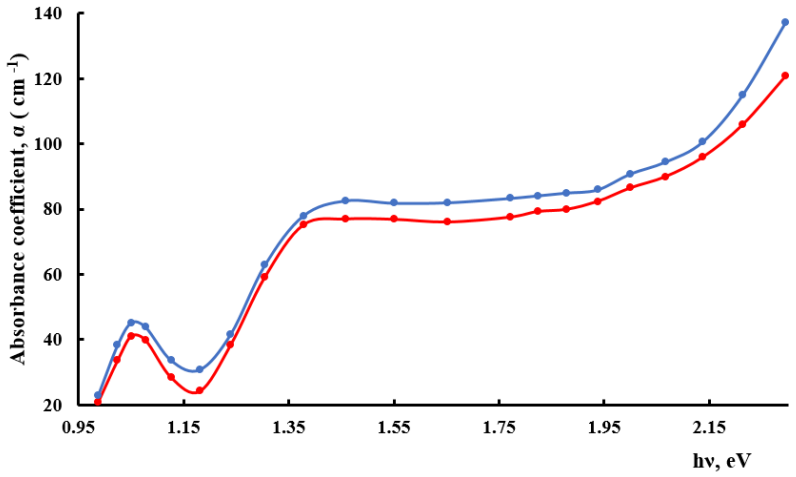

Fig. 4. Absorption spectra of the $Ga_{0.997}B_{0.003}Se$ crystal at 300 K (1) and 110 K (2)

To establish a more complete understanding of the optical response of boron-doped GaSe crystals, the spectral dependence of photocurrent for $Ga_{1-x}B_xSe$ (x = 0.3% and 0.5%) was measured at 295 K (Fig. 5). For $Ga_{0.997}B_{0.003}Se$ (Fig. 5a), the spectral shape changes considerably: the dominant photocurrent peak appears at 1.77 eV, while the long-wavelength edge extends to about 0.9 eV. This red-shift of the principal maximum relative to the fundamental absorption edge (≈ 1.96 eV) reflects the activation of boron-induced acceptor levels, which enable transitions of thermally excited electrons from localized states to the conduction band. The broadening of the spectral response further suggests the involvement of defect-related states in the photo generation process. For $Ga_{0.995}B_{0.005}Se$ (Fig.5b), the main photocurrent peak shifts slightly toward higher energy (≈ 1.95 eV) and the overall photocurrent amplitude decreases. This trend can be attributed to enhanced radiative recombination and a partial reduction in the density of localized impurity states at higher boron concentration. The observed spectral behavior indicates a competition between optical absorption and carrier recombination processes, consistent with the temperature-dependent absorption characteristics discussed earlier.

Overall, the close correspondence between the absorption edge (~ 1.96 eV) and the photocurrent maxima confirms that boron incorporation modifies both the optical and electrical photo response of GaSe in a correlated manner. Such correlation between absorption and photoconductivity spectra provides deeper insight into the role of boron-induced impurity levels in determining the carrier excitation and recombination mechanisms, thus supporting the potential of $Ga_{1-x}B_xSe$ crystals for broadband photodetector applications.

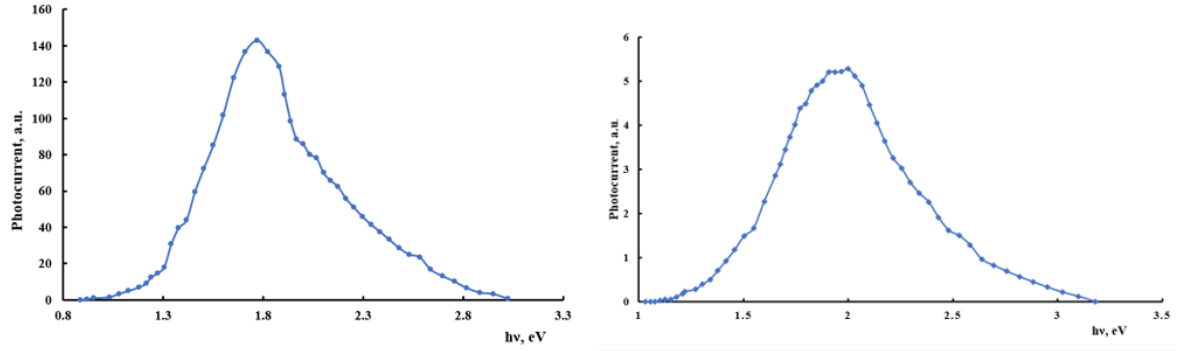

a) **b)**

Fig. 5. Photoconductivity spectra of $Ga_{1-x}B_xSe$ single crystals at 295 K: (a) x = 0.3% and (b) x = 0.5%.

4. Conclusion

In this study, single crystals of $Ga_{1-x}B_xSe$ (x = 0.3% and 0.5%) were successfully synthesized by the horizontal Bridgman method, and their optical and photoelectrical properties were systematically investigated. The incorporation of boron into the GaSe lattice led to distinct modifications in the electronic band structure and photo response behavior. UV–Vis absorption studies revealed a slight narrowing of the direct band gap from 2.0 eV for pure GaSe to approximately 1.960–1.963 eV for boron-doped samples, which effectively extended the optical absorption edge toward the longer-wavelength (visible–NIR) region. This band gap tuning occurred without degradation of crystalline quality, demonstrating that boron doping provides an effective means for tailoring the spectral sensitivity of GaSe-based materials. The appearance

of additional absorption features at 1.05 eV and 1.35 eV indicated the formation of boron-induced impurity states within the band gap. These localized levels were found to play a crucial role in determining the temperature-dependent optical behavior — at lower boron content, the absorption coefficient increased with temperature due to thermal excitation of carriers, whereas at higher boron concentration, enhanced radiative recombination resulted in a negative temperature coefficient of absorption. Photoconductivity measurements further confirmed the close relationship between the optical absorption and carrier excitation processes. The photocurrent spectra exhibited a strong peak at 1.77 eV for $Ga_{0.997}B_{0.003}Se$ and at 1.95 eV for $Ga_{0.995}B_{0.005}Se$, consistent with the absorption edge obtained from optical measurements. The red-shift and spectral broadening observed in the lower-doped sample reflected transitions involving boron-related acceptor levels and defect states, while the blue-shift and reduced amplitude at higher doping indicated increased recombination losses. These results clearly demonstrate a strong correlation between the optical absorption and photoconductivity spectra, highlighting the impact of boron incorporation on carrier generation and recombination mechanisms.

Overall, the findings confirm that controlled boron substitution provides an efficient approach for engineering the band structure and photo response of GaSe without compromising its layered crystalline nature. The combined optical and photoconductivity analyses reveal that $Ga_{1-x}B_xSe$ crystals possess tunable optoelectronic characteristics, making them highly promising materials for broadband photodetectors and other next-generation optoelectronic devices operating in the visible and near-infrared spectral regions.

REFERENCE LIST

26. Bastow, T. J., Campbell, I. D., & Whitfield, H. J. (1981). A 69Ga, 115In NQR study of polytypes of GaS, GaSe and InSe. Solid State Communications, 39(2), 307-311.
27. He, Z., Guo, J., Li, S., Lei, Z., Lin, L., Ke, Y., ... & Zhang, X. (2020). GaSe/MoS2 heterostructure with ohmic-contact electrodes for fast, broadband photoresponse, and self-driven photodetectors. Advanced Materials Interfaces, 7(9), 1901848.
28. Abderrahmane, A., Jung, P. G., Kim, N. H., Ko, P. J., & Sandhu, A. (2017). Gate-tunable optoelectronic properties of a nano-layered GaSe photodetector. Optical Materials Express, 7(2), 587-592.
29. Hu, P., Wen, Z., Wang, L., Tan, P., & Xiao, K. (2012). Synthesis of few-layer GaSe nanosheets for high performance photodetectors. ACS nano, 6(7), 5988-5994.
30. Curreli, N., Serri, M., Zappia, M. I., Spirito, D., Bianca, G., Buha, J., ... & Bonaccorso, F. (2021). Liquid-phase exfoliated gallium selenide for light-driven thin-film transistors. Advanced Electronic Materials, 7(3), 2001080.
31. Kumar, A. S., Wang, M., Li, Y., Fujita, R., & Gao, X. P. (2020). Interfacial Charge Transfer and Gate-Induced Hysteresis in Monochalcogenide InSe/GaSe Heterostructures. ACS Applied Materials & Interfaces, 12(41), 46854-46861.
32. Tao, H., Fan, Q., Ma, T., Liu, S., Gysling, H., Texter, J., ... & Sun, Z. (2020). Two-dimensional materials for energy conversion and storage. Progress in Materials Science, 111, 100637.
33. Ertap, H. (2018). Nonlinear absorption, SHG behavior and carrier dynamics of Nd and Pr doped GaSe single crystals. Optical Materials, 83, 99-103.
34. Bassou, A., Rajira, A., El Kanouny, A., Abounadi, A., El Haskouri, J., & Almaggoussi, A. (2021). Optical properties of GaSe, characterization and simulation. Materials Today: Proceedings, 37, 3789-3792.
35. Zalamai, V. V., Stamov, I. G., & Syrbu, N. N. (2021). Interference of exciton-polariton waves in GaSe nanocrystals. Materials Today Communications, 27, 102355.

36. Wu, Y., Fuh, H. R., Zhang, D., Coileáin, C. Ó., Xu, H., Cho, J., ... & Wu, H. C. (2017). Simultaneous large continuous band gap tunability and photoluminescence enhancement in GaSe nanosheets via elastic strain engineering. Nano Energy, 32, 157-164.
37. Bassou, A., Rajira, A., El-Hattab, M., El Haskouri, J., Murcia-Mascaros, S., Almaggoussi, A., & Abounadi, A. (2022). Structural and optical properties of a layered ε-GaSe thin film under elastic deformation from flexible PET substrate. Micro and Nanostructures, 163, 107152.
38. Huang, L., Chen, Z., & Li, J. (2015). Effects of strain on the band gap and effective mass in two-dimensional monolayer GaX (X= S, Se, Te). Rsc Advances, 5(8), 5788-5794.
39. Ma, Y., Dai, Y., Guo, M., Yu, L., & Huang, B. (2013). Tunable electronic and dielectric behavior of GaS and GaSe monolayers. Physical Chemistry Chemical Physics, 15(19), 7098-7105.
40. Rybkovskiy, D. V., Arutyunyan, N. R., Orekhov, A. S., Gromchenko, I. A., Vorobiev, I. V., Osadchy, A. V., ... & Obraztsova, E. D. (2011). Size-induced effects in gallium selenide electronic structure: The influence of interlayer interactions. Physical Review B—Condensed Matter and Materials Physics, 84(8), 085314.
41. Lei, S., Ge, L., Liu, Z., Najmaei, S., Shi, G., You, G., ... & Ajayan, P. M. (2013). Synthesis and photoresponse of large GaSe atomic layers. Nano letters, 13(6), 2777-2781.
42. Wang, C., Yang, S. X., Zhang, H. R., Du, L. N., Wang, L., Yang, F. Y., ... & Liu, Q. (2016). Synthesis of atomically thin GaSe wrinkles for strain sensors. Frontiers of Physics, 11(2), 116802.
43. Wang, Z., Wei, X., Huang, Y., Zhang, J., & Yang, J. (2023). High solar-to-hydrogen efficiency in AsP/GaSe heterojunction for photocatalytic water splitting: A DFT study. Materials Science in Semiconductor Processing, 159, 107393.
44. Li, X., Bao, A., Guo, X., Ye, S., Chen, M., Hou, S., & Ma, X. (2023). A type-II GaP/GaSe van der Waals heterostructure with high carrier mobility and promising photovoltaic properties. Applied Surface Science, 618, 156544.
45. Bassou, A., Rajira, A., Gil, B., Almaggoussi, A., & Abounadi, A. (2023). Accurate determination of optical parameters of non transparent materials: The ε–GaSe case. Optical Materials, 140, 113887.
46. Kępińska, M., Nowak, M., Duka, P., & Kauch, B. (2009). Spectrogoniometric determination of refractive indices of GaSe. Thin Solid Films, 517(13), 3792-3796..
47. Chen, Y., Sun, Y., Dai, X., Zhang, B., Ye, Z., Wang, M., & Wu, H. (2015). Tunable electrical properties of NiO thin films and p-type thin-film transistors. Thin Solid Films, 592, 195-199.
48. Garcés, F. A., Budini, N., Arce, R. D., & Schmidt, J. A. (2015). Effect of thickness on structural and electrical properties of Al-doped ZnO films. Thin solid films, 574, 162-168.
49. Muydinov, R., Steigert, A., Schönau, S., Ruske, F., Kraehnert, R., Eckhardt, B., ... & Szyszka, B. (2015). Water-assisted nitrogen mediated crystallisation of ZnO films. Thin Solid Films, 590, 177-183.
50. Wang, Y., Capretti, A., & Dal Negro, L. (2015). Wide tuning of the optical and structural properties of alternative plasmonic materials. Optical Materials Express, 5(11), 2415-2430.
51. Pankove, J. I. (1971). Optical processes in semiconductors Prentice-Hall. New Jersey, 92, 36.
52. Andres-Penares, D., Cros, A., Martinez-Pastor, J. P., & Sanchez-Royo, J. F. (2017). Quantum size confinement in gallium selenide nanosheets: band gap tunability versus stability limitation. Nanotechnology, 28(17), 175701.
53. Guseinov, A. G., Salmanov, V. M., Mamedov, R. M., Salmanova, A. A., & Akhmedova, F. S. (2017). Optical Properties of Boron-Doped Gallium Selenide. Optics and Spectroscopy, 123(6), 875-880.
54. Agekyan V.F., Grigorieva N.R. (2016). Luminescence of semiconductor crystals. St. Petersburg: Publishing house of St. Petersburg University, 2016. 156 p.

JOURNAL OF BAKU ENGINEERING UNIVERSITY - PHYSICS
2025. Volume 9, Number 1 *Pages 43-51*

UDC: 620.91:536.7
DOI: https://doi.org/10.30546/09081.2025.001.8038

UTILIZING THERMAL WATER FOR ENERGY: A STUDY OF THE PROPERTIES (P, P, T) OF THE "KHACHMAZ" THERMAL WATER IN AZERBAIJAN

Mahir BASHIROV
Department of Mechanical Engineering Baku Engineering University
Baku, Azerbaijan
mbashirov@beu.edu.az

Natig RZAYEV
Department of Mechanical Engineering Baku Engineering University
Baku, Azerbaijan
nrzayev@beu.edu.az

Nofal NABIYEV
Department of Mechanical Engineering
Baku Engineering University
Baku, Azerbaijan
nnabiyev@beu.edu.az

Aytan NAMAZOVA
Technical-Humanitarian Lyceum
Baku, Azerbaijan
aytan_bashirova@yahoo.com

ARTICLE INFO

Article history
Received:2025-06-21
Received in revised form:2025-06-24
Accepted:2025-11-18
Available online

Keywords:
energy, power plants, thermal waters, viscosity, density

ABSTRACT

This study investigates the potential of using thermal waters for energy production and presents a table showing the role of thermal power plants in global electricity generation. Additionally, an experimental study was conducted on the properties (pressure, density, temperature) of the "Khachmaz" thermal water from Azerbaijan. To evaluate the performance and accuracy of the experimental apparatus, the measured properties (p, ρ, T) of water, toluene, and an aqueous NaCl solution ($m = 2.96661$ mol·kg^{-1}) were compared with reference data from various literature sources. The results obtained are displayed in graphical form.

I. INTRODUCTION

Thermal waters, which naturally emerge from the ground, are utilized for various purposes, including the generation of environmentally friendly and cost-effective electricity, the treatment of various diseases, heating of buildings, greenhouses, and small agricultural enterprises, as well as providing heat for facilities operating with natural steam. Additionally, these waters, containing high concentrations of diverse salts, are used for the extraction of mineral substances and therapeutic applications. This, in turn, fosters the development of various industries such as

hotels, motels, campsites, catering services, communication networks, and infrastructure in regions with abundant thermal water resources. As a result, the country's state budget receives a large amount of funds, creating conditions for a positive solution to the unemployment problem [1].

In accordance with the State Program on the Use of Alternative and Renewable Energy Sources, the Ministry of Energy was tasked with implementing a special program, as specified in the Decree of the Republic of Azerbaijan dated October 21, 2004 [1]. In the State Program, the use of wind energy is emphasized, along with energy sources that are suitable for our republic. These include solar energy, geothermal water, hydropower from mountain rivers and canals, and biomass energy. There are significant possibilities for utilizing the heat from the Earth's depths. Depending on its temperature, water or a water-steam mixture can be used for hot water supply, heating, electricity generation or for all of these purposes simultaneously. It is more suitable to utilize the high-temperature heat from volcanic regions and dry mountain rocks for electricity generation and heat supply. The total operational capacity of geothermal power plants worldwide remains behind that of most other renewable energy sources. However, in specific populated geographic regions where fuel and mineral resources are either nonexistent or relatively expensive, the high energy density, in conjunction with government policies, is driving the advancement of this sector.

The temperature of mineral waters in Azerbaijan ranges from 4 to 65°C. This refers only to natural water sources. Additionally, waters with temperatures reaching 95°C are extracted by drilling deep into the earth.

II.Description of the Processing System

Thermal waters are commonly used worldwide for electricity generation through thermal power plants (TPPs) [2]. This type of power plant has the advantage of requiring less time and fewer financial resources for construction compared to other types of power plants. Electricity from geothermal power plants is 70-80% cheaper than that from thermal power plants relying on oil, gas, or coal. Such power plants have a negligible environmental impact, with the electricity they generate being notably cleaner from an ecological perspective compared to that produced by other types of power stations. The CO2 emissions associated with the generation of 1 kW of electricity from high-temperature thermal sources vary between 13 and 380 grams, with an average of 65 grams per kilowatt-hour. When using different fuels, this index measures 453 grams for natural gas, 906 grams for oil, and 1042 grams for coal. The chemical compounds generated by thermal flow are carefully contained and not allowed to escape into the atmosphere. Instead, they are efficiently redirected back into the earth’s depths using advanced specialized devices [3-4].

The primary requirement for developing Thermal Power Plants is the presence of high-temperature thermal waters that emerge from the ground, with an efficiency exceeding 90%. Therefore, given the advantages of thermal power stations (TPP) over other types of power plants and the low cost of energy procurement, regions such as Latin America, Northern Europe, and Northern Africa—which are endowed with abundant hydropower resources—place significant emphasis on the development of thermal stations. This is regarded as one of the most promising sectors for these countries. The global electricity generation from thermal power plants has experienced significant growth, increasing from 5,000 MW in 1990 to approximately 11,000 MW in 2010. In the same year, thermal power plants contributed to 30% and 27% of the

total electricity generated in Iceland and the Philippines, respectively, while accounting for 14% each in El Salvador and Costa Rica [5-6].

In general, for the first time in the world, heat was obtained from thermal waters in Italy in 1904, and similar power plants were built in New Zealand, Japan, the Philippines and the United States in the following years.

Russia has significant geothermal resources distributed across various regions, including Kamchatka, Chukotka, Primorsky Krai, Western Siberia, the North Caucasus, Krasnodar and Stavropol Territories, as well as the Kaliningrad Oblast. In these regions, thermal waters emerge from multiple hot sources ranging from 50 to 90°C. More than 100 natural thermal water outlets are known in Kamchatka. The sources are distinguished not only by their high temperature (170-200^0 C) but also by their relatively low mineral content. Significant reserves of highly thermal waters (temperature over 100°C, depth 1500 m) are located in the artesian basins of Moscow and Western Siberia.

Table 1 clearly demonstrates the significant share of thermal power plants in total electricity production for the years 2007 and 2010 across the 12 most developed countries operating thermal power plants in the world [5,6].

The United States stands as the global leader in electricity production from thermal power plants. In 2007, the country generated an impressive 2,687 MW of electricity from thermal energy, further increasing to 3,086 MW in 2010. Notably, in 1999, the utilization of thermal energy saved an astonishing 60,000 barrels of oil. During that same year, the production from thermal sources reached 2,200 MW, equivalent to the output of four nuclear power plants. This demonstrates the significant role thermal energy plays in the nation's energy landscape [7].

III.Performance Improvement

Iceland leads the world in utilizing geothermal resources, employing thermal waters for heating the capital city Reykjavík, as well as for residential needs, public utilities, greenhouse operations, and the production of environmentally sustainable electricity.

Despite having abundant thermal water resources, Azerbaijan utilizes only a small fraction of them. Based on usability, geostructural, and hydro-geothermal conditions, the hydrothermal regions include Greater Caucasus, Absheron Peninsula, Caspian-Guba, Kur-Araz Lowland, Lesser Caucasus, Talysh-Lankaran, Jalilabad-Zar, Shamakhi-Gobustan, Ajinohur-Kur Interfluve, and Nakhchivan. The thermal regions of Azerbaijan have reserves totaling 249 thousand m^3/day; however, a significant portion of these reserves is utilized for treatment purposes [8].

TABLE I. THE CONTRIBUTION OF THERMAL POWER PLANTS TO GLOBAL ELECTRICITY PRODUCTION WAS ANALYZED FOR THE YEARS 2007 AND 2010

№	Countries utilizing thermal power plants	Capacity of thermal power plants, MW		The proportion of electricity generated by TPP in the overall electricity output of the country, expressed as a percentage
		In 2007 [5]	In 2010 [6]	
1.	USA	2687	3086	0,3
2.	Philippines	1969,7	1904	27
3.	Indonesia	992	1197	3,7
4.	Mexico	953	958	3,0
5.	Italy	810,5	843	-
6.	New Zealand	471,6	628	10,0
7.	Iceland	421,2	575	30,0
8.	Japan	535,2	536	0,1
9.	Salvador	204,2	204	14,0
10.	Kenya	128,8	167	11,2
11.	Costa Rica	162,5	166	14,0
12.	Nicaragua	87,4	88	10,0
	Total	9423,1	10352	

The thermal waters in Absheron are primarily used for restoring the health of the population and treating various diseases. If the Surakhani thermal water, which has significant potential, is utilized effectively, it could generate substantial revenue for the republic's budget. For comparison, it is worth noting that thermal water with a temperature of 71°C emerges in the center of Budapest, the capital of Hungary. This water is cooled to 30-35°C and is utilized daily by 4-5 thousand people at the Széchenyi Thermal Baths, a complex of indoor and outdoor pools located in the Széchenyi area of the city. Each person's daily access fee for using this thermal water facility is 12 euros. The daily revenue from this operation amounts to 54,000 euros, while the annual revenue reaches 19.5 million euros.

Considering the numerous thermal water resources with a temperature of 30-35°C in the Gabala, Gakh, Oghuz, and Guba administrative regions, we consider it appropriate to create closed and open-type beaches in these areas. The presence of rich oil and gas reserves in the territory of the economic-geographic region, the continuation of tectonic events and orogeny processes, and the fact that it is surrounded by the Caspian Sea in a large area are the main factors for the existence of a large number of thermal and mineral waters here (Fig. 1) [9]. This region lags behind only Absheron and Lankaran-Astara economic-geographic regions in terms of the use of thermal and mineral waters for the restoration of human health, as well as the use of beaches.

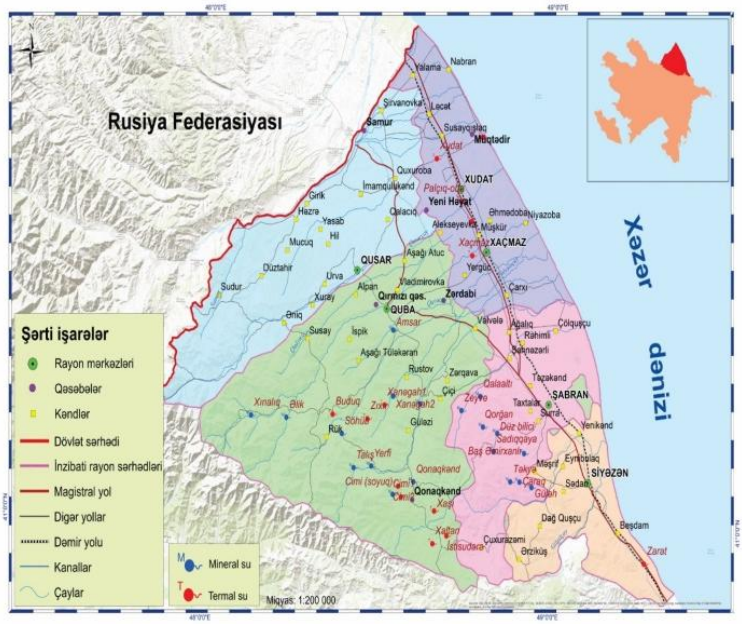

Fig. 1. Map illustrating the thermal and mineral water resources of the Guba-Khachmaz economic-geographical region

Azerbaijan has many favorable opportunities for developing thermal power stations, but none have been built yet. Although Azerbaijan possesses abundant oil and gas resources, these are classified as non-renewable assets. Therefore, leveraging the historically established experience of utilizing thermal waters worldwide should be considered one of the most critical priority areas for Azerbaijan. Considering the substantial reserves of high-temperature thermal waters in various administrative regions of the Republic of Azerbaijan, and their immense potential for the cost-effective and environmentally friendly generation of electricity, strategic emphasis should be placed on advancing this sector, particularly in regions of the republic that face deficiencies in fuel supply, energy infrastructure, and hydroelectric capacity. The percentage of thermal and mineral waters in the Guba-Khachmaz economic-geographic region, categorized by administrative district, is presented in Fig. 2 [9].

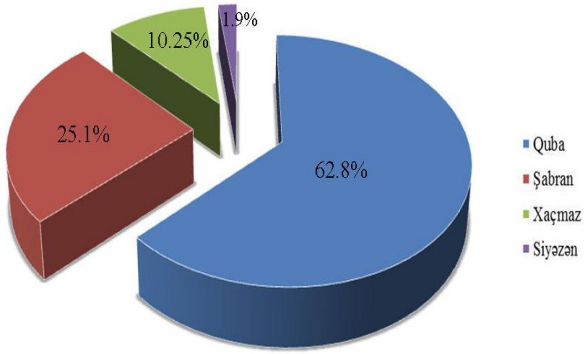

Considering the above, we can draw the following conclusion:

1. The initiatives undertaken in Azerbaijan to harness electricity from thermal waters, an inexhaustible natural resource, have thus far proven insufficient.
2. The lack of detailed information regarding the exact number of high-temperature thermal water sources in Azerbaijan, along with their flow rates and potential applications, poses a significant obstacle to the development of thermal power plants within the republic.

3. Given the favorable conditions for constructing power plants using high-temperature thermal waters in Azerbaijan, it would be beneficial to develop such facilities. This approach could help meet the growing electricity demand in the country's regions, utilizing best practices from around the world to harness this inexhaustible resource effectively.
4. Foreign investors in Azerbaijan are allocating significant financial resources to develop various economic sectors. By encouraging both foreign and local entrepreneurs to participate in the construction of thermal power plants, which require relatively low financial investment, the utilization of thermal waters in the power industry can be effectively advanced. Geothermal technologies, at various stages of development worldwide, are widely utilized in central heating systems, greenhouses, and other applications. The technology for generating electricity from naturally high-permeability hydrothermal reservoirs is considered reliable. Most of the geothermal power plants currently operating worldwide utilize dry steam turbines or "flash" units (including single, double, and triple flash systems) and rely on hot water sources that exceed 180°C. Additionally, new technologies such as "Enhanced Geothermal Systems (EGS)" are under development and moving towards implementation.

Another type of geothermal power plant utilizes natural geothermal resources, which consist of water heated to high temperatures through natural processes. However, the availability of such resources is limited. For instance, in Russia, regions like Kamchatka and the Caucasus are known for their mineral water sources. In this system, heated water is drawn from the ground and enters a heat exchanger. In another case, water rises freely through a specially drilled well due to high geological pressure. This general operating principle is applicable to nearly all types of geothermal power plants.

The thermal waters under investigation were directly collected from their surface discharge zones and processed using various chemical treatment methods for experimental purposes. These locations are rich in both thermal and cold mineral springs, which contain nitrogen and hydrogen sulfide. In the "Khachmaz" geothermal energy resource of the Khachmaz region in Azerbaijan, sodium (Na) is the predominant chemical element. It constitutes approximately 72.41–90.12% of all chemical substances found in the composition of the "Khachmaz" geothermal energy resource in Azerbaijan's Khachmaz region. [10,11].

Prior to conducting the main experiments, the functionality of the experimental apparatus was evaluated through verification experiments using substances with well-documented experimental data. Given that the vibrating tube method requires calibration with at least three substances, water, toluene, and NaCl aqueous solutions were chosen as the primary calibrators for this purpose. The calibration process was subsequently analyzed in detail. Following the calibration of the device, repeated measurements were conducted using the selected calibrating substances to ensure the reliability and precision of the calibration process. In some cases, experiments were conducted 4-5 times at the same temperatures, and the device's performance was evaluated at different times, regardless of variations in its filling and experimental conditions. The laboratory in which the experiments were conducted was maintained at a constant temperature of T = 293.15 K under climate-controlled conditions. A comparative analysis of the results obtained for aqueous solutions of water, toluene, and NaCl (m = 2.96661 mol·kg^{-1}) with the corresponding values reported in the literature is presented in Figures 1, 2, and 3.

As illustrated in the figures below, the discrepancy between the newly obtained density data and the values reported in the literature does not exceed the estimated measurement errors associated with this device. Double-distilled water was obtained from different laboratory facilities. NaCl, toluene, and other chemicals were sourced from Merck (Germany). Consistently, the results obtained were in close agreement with minimal error. All of this demonstrates the high accuracy of the constructed experimental device.

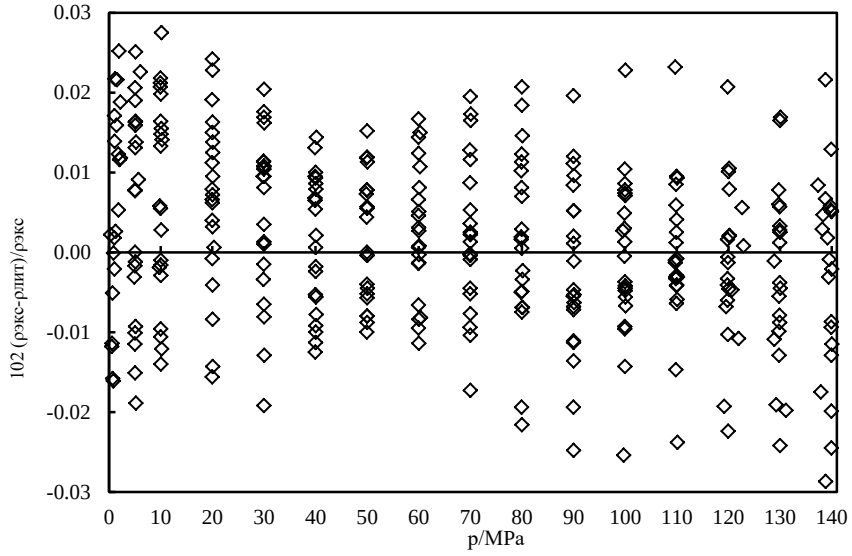

Fig. 1. The pressure dependence of the measured density of water at temperatures T=(278.15–468.15) K and its deviation from the IAPWS 95 data reported in the literature.

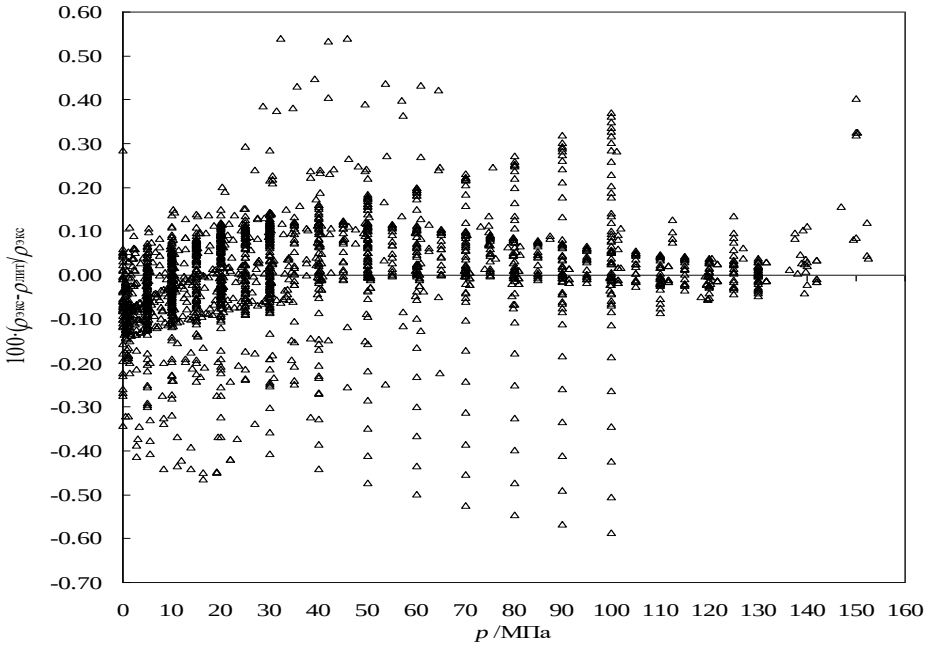

Fig. 2. The pressure dependence of the measured density of toluene at temperature T=(278.15-468.15) K and along with comparisons to data found in various literature sources up to the year 2000.

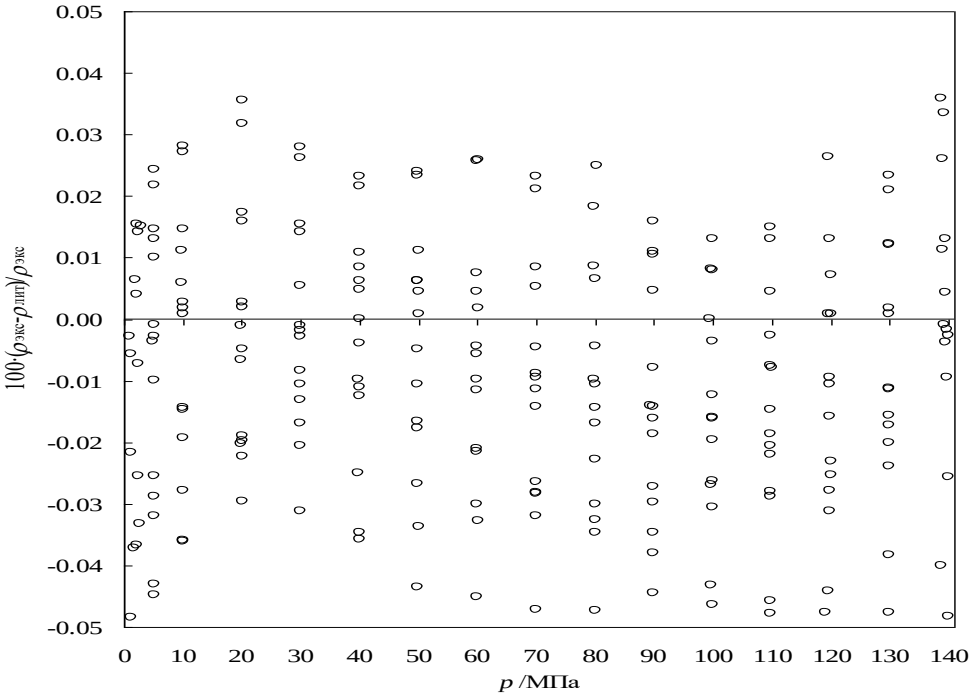

Fig. 3. The pressure dependence of the measured density of an aqueous solution of NaCl (m=2,96661 mol·kq^{1}) at temperature T=(278.15-468.15) K and along with comparisons to data found in various literature sources up to the year 2000.

After performing verification experiments on water, NaCl, and toluene (p, ϱ, T), the pressure, density, and temperature dependencies of Azerbaijan's 'Khachmaz' thermal water were systematically measured at elevated pressures and varying temperatures using the vibrating tube method in the experimental setup.

During the measurement of the (p, ϱ, T) dependencies at each equilibrium state, efforts were made to achieve the lowest possible pressure values. This approach was intended to obtain highly accurate density values through graphical extrapolation to atmospheric pressure and extrapolated density values were subsequently compared with measurements obtained using the DMA 4500 device. The data obtained from these methods are in good agreement, with a variation of ±0.02%. Experiments were conducted at pressure intervals of approximately 5 MPa for each isotherm. For all studied subjects, the research was performed at temperatures ranging from T = (278.15 K ÷373.15 K), and pressures up to p = 40 MPa. The experimental values of pressure (p), density (ϱ), and temperature (T) are presented in Table 2.

TABLE II. THE EXPERIMENTAL EVALUATION OF THE DENSITY OF "KHACHMAZ" THERMAL WATER FROM AZERBAIJAN'S KHACHMAZ REGION AT VARYING PRESSURES AND TEMPERATURES

$\frac{\text{p}}{\text{MPa}}$	$\frac{\rho}{kq/m^3}$	$\frac{\text{T}}{\text{K}}$	$\frac{\text{p}}{\text{MPa}}$	$\frac{\rho}{kq/m^3}$	$\frac{T}{\text{K}}$
0.624	1004.04	278.15	1.160	989.32	328.02
5.004	1006.21	278.15	5.024	990.99	328.04
10.023	1008.65	278.16	10.079	993.00	328.17
15.012	1011.05	278.15	15.576	995.38	328.18
20.035	1013.43	278.14	19.985	997.22	328.19
25.036	1015.76	278.15	25.527	999.61	328.17
30.054	1018.07	278.15	30.023	1001.50	328.14
35.124	1020.37	278.14	35.513	1003.58	328.12
40.021	1022.56	278.15	39.978	1005.37	328.06
0.539	1002.59	288.14	0.846	981.22	343.15
5.006	1004.66	288.16	5.097	983.06	343.16
9.855	1006.87	288.17	9.967	985.17	343.14
15.151	1009.25	288.17	15.525	987.55	343.15
20.064	1011.43	288.17	20.000	989.45	343.15
25.121	1013.64	288.16	25.586	991.82	343.14
30.103	1015.79	288.16	30.045	993.68	343.16
35.111	1017.92	288.16	35.514	995.98	343.15
40.145	1020.04	288.15	40.050	997.87	343.15
1.025	1000.15	298.27	0.846	974.29	354.24
5.079	1002.02	298.22	5.097	976.23	354.25
9.818	1004.22	298.22	9.967	978.33	354.27
15.593	1006.61	298.17	15.525	980.63	354.27
20.018	1008.46	298.13	20.000	982.58	354.27
25.104	1010.69	298.13	25.586	984.92	354.27
30.155	1012.85	298.12	30.045	986.83	354.28
35.089	1014.82	298.13	35.514	989.17	354.27
40.040	1016.88	298.13	40.050	991.07	354.27
0.898	995.52	313.08	1.626	962.02	372.90
4.995	997.25	313.10	5.059	963.59	372.90
9.972	999.20	313.15	10.042	965.73	372.96
15.563	1001.65	313.17	15.525	968.08	372.97
20.008	1003.42	313.20	20.014	970.00	372.99
25.534	1005.80	313.18	25.596	972.31	373.00
30.057	1007.65	313.19	30.001	974.44	372.90
35.586	1009.82	313.17	35.576	976.79	372.91
39.970	1011.52	313.15	40.013	978.53	372.92

Isotherms were constructed in the pressure-density (p-ϱ) coordinates for pressure values ranging from 0.1 to 40 MPa, as illustrated in Figure 4.

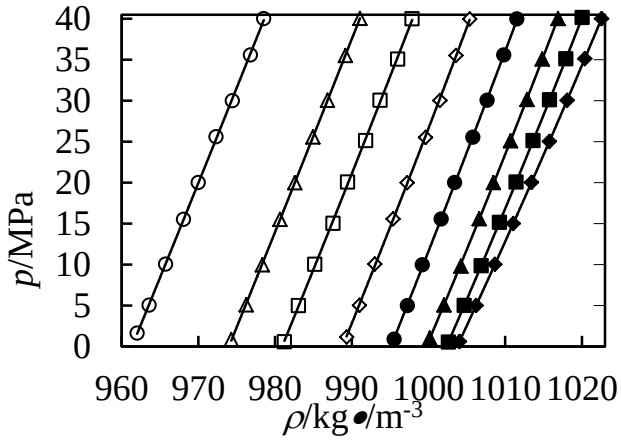

Fig. 4. The relationship between pressure (p) and density (ϱ) of the "Khachmaz" thermal water in the Khachmaz region of Azerbaijan was calculated using formulas 1 and 2.

♦, 278,15 K; ■, 288,16 K; ▲, 298,17 K; •, 313,18 K; ◊, 328,18 K;□, 343,15 K; Δ, 354,27 K; ○, 372,96 K.

IV.Conclusion

The measured density of "Khachmaz" thermal water of Khachmaz region of Azerbaijan was also measured at atmospheric pressure with an accuracy of 0.01% (more accurate than at high pressures) on a DMA 5000M device. This device enables precise measurements at temperatures up to T=363,15 K. The results obtained are expressed using the following equation of state:

$$p = A\rho^2 + B\rho^8 + C\rho^{12} \quad (1)$$

Adding a third term to the Akhundov-Imanov equation has been shown to reduce the error in describing experimental data to $\Delta\varrho/\varrho=\pm$(0.001 to 0.003)%. The coefficients A(T), B(T), and C(T) are functions of temperature and can be expressed in polynomial form:

The values of the coefficients a_{ij}, b_{ij}, and c_{ij} in the equation $A(T) = \sum_{i=1}^{3} a_i T^i$, $B(T) = \sum_{i=0}^{2} b_i T^i$,

$$C(T) = \sum_{i=0}^{2} c_i T^i$$

are given in Table 3.

TABLE III.

a_1= -3.9508587	b_0= 8322.6444921	c_0= -6583.286607275
a_2= 0.019210690563	b_1= -56.828468335	c_1= 45.23492762848
a_3= -0. 3685081337·10^{-4}	b_2= 0.103286734291	c_2= -0.07893862924

Equation (1), considering the values of the coefficients A(T), B(T), and C(T), allows for the empirical determination of the dependency of the "Khachmaz" thermal water on (p, ϱ, T) with an average error of 0.007%.

REFERENCES

[1] The State Program on Use of Alternative and Renewable Energy Sources in Azerbaijan Republic (approved by the order of the President of the Azerbaijan Republic, no. 462 dated October 21, 2004)

[2] "Methods for measuring the thermal-physical properties of geothermal energy sources in the Khachmaz region, Republic of Azerbaijan", Baku – "Science" – 2013

[3] Namazova A.M. Thermal waters of the Greater Caucasus and their rational use // Bulletin of modern science. Scientific-theoretical journal, Volgograd: 2015, No. 4, pp. 178-181

[4] Namazova A.M. "Utilization of thermal waters in electric energy industry in the world and in Azerbaijan" Proceedings of the Azerbaijan Geographical Society. Geography and natural resources, 2015, No. 2, pp. 119-121

[5] Online resources: www.eco.gov.az; www.az.wikipedia.org; https://www.renewable.com/; http://topnews.az/news/439714/ www.//ru/wikipedia/org/wiki/геотермальная_энергетика

[6] Bertani, Ruggero (September 2007) "Wordl Geothermal Generation in 2007", Geo-Heat Centre Quarterly Bulletin (Klamath Falls, Oregon: Oregon Institute of Technology). T.28 (3): s.8-19, ISSN 0276-1084

[7] Holm, Alison (May 2010), "Geothermal Energy: International Market Update", Geothermal Energy Association, cc. 7

[8] Namazova A.M. Economic significance of mineral and thermal waters of the Sheki-Zagatala economic-geographical region // Baku University News. Natural Sciences Series, 2015, No. 3, pp. 152-159.

[9] Namazova A.M. Thermal and mineral water of Guba-Khachmaz economic region,their rational use opportunities // Proceedings of young scientists. 2016, No 13, p.61-68

[10] N.D.Nabiev, M.M.Bashirov, J.T.Safarov, A.N.Shahverdiyev, E.P.Hassel "Thermodynamic properties of geothermal energy resources (Khachmaz Sabir-Oba) of Azerbaijan" Journal of Chemical and Engineering data, Vol. 54,No.6, 2009.

[11] N.D.Nabiev "Study of thermal-physical properties of geothermal energy resources of the Khachmaz region of Azerbaijan." Dissertation submitted for the degree of Doctor of Philosophy in Engineering, Baku, 2011, 177 pages.

[12] Akhundov T.S., Imanov Sh.Y. Equation of State for Ortho- and Paraxylene // Proceedings of Higher Educational Institutions, Oil and Gas, 1969, No. 12, p. 24.

INSTRUCTIONS FOR AUTHORS

1. "The Baku Engineering University Journal-Physics" accepts original unpublished articles and reviews in the research field of the author.
2. Articles are accepted in English.
3. File format should be compatible with **Microsoft Word** and must be sent to the electronic mail (**journal@beu.edu.az**) of the Journal. The submitted article should follow the following format:

- Article title, author's name and surname
- The name of workplace
- Mail address
- Abstract and key words

4. The title of the article should be in each of the three languages of the abstract and should be centred on the page and in bold capitals before each summary.
5. **The abstract** should be written in **9 point** type size, between **100** and **150** words. The abstract should be written in the language of the text and in two more languages given above. The abstracts of the article written in each of the three languages should correspond to one another. The keywords should be written in two more languages besides the language of the article and should be at least three words.
6. **UDC** and **PACS** index should be used in the article.
7. The article must consist of the followings:

- Introduction
- Research method and research
- Discussion of research method and its results
- In case the reference is in Russian it must be given in the Latin alphabet with the original language shown in brackets.

8. **Figures, pictures, graphics and tables** must be of publishing quality and inside the text. Figures, pictures and graphics should be captioned underneath, tables should be captioned above.
9. **References** should be given in square brackets in the text and listed according to the order inside the text at the end of the article. In order to cite the same reference twice or more, the appropriate pages should be given while keeping the numerical order. For example: [7, p.15].

Information about each of the given references should be full, clear and accurate. The bibliographic description of the reference should be cited according to its type (monograph, textbook, scientific research paper and etc.) While citing to scientific research articles, materials of symposiums, conferences and other popular scientific events, the name of the article, lecture or paper should be given.

Samples:

a) ***Article:*** Demukhamedova S.D., Aliyeva İ.N., Godjayev N.M.. *Spatial and electronic structure af monomerrik and dimeric conapeetes of carnosine üith zinc,* Journal of structural Chemistry, Vol.51, No.5, p.824-832, 2010

b) ***Book:*** Christie ohn Geankoplis. *Transport Processes and Separation Process Principles*. Fourth Edition, Prentice Hall, p.386-398, 2002

c) ***Conference paper:*** Sadychov F.S., Aydın C., Ahmedov A.İ.. Appligation of Information – Commu-nication Technologies in Science and education. II International Conference."*Higher Twist Effects In Photon- Proton Collisions", Bakı, 01-03 Noyabr, 2007, ss 384-391*
References should be in 9-point type size.

10. The margins sizes of the page: - Top 2.8 cm. bottom 2.8 cm. left 2.5 cm, right 2.5 cm. The article main text should be written in Palatino Linotype 11 point type size single-spaced. Paragraph spacing should be 6 point.
11. The maximum number of pages for an article should not exceed 15 pages
12. The decision to publish a given article is made through the following procedures:

- The article is sent to at least to experts.
- The article is sent back to the author to make amendments upon the recommendations of referees.
- After author makes amendments upon the recommendations of referees the article can be sent for the publication by the Editorial Board of the journal.